

ASPIRE: Iterative Amortized Posterior Inference for Bayesian Inverse Problems

Rafael Orozco¹, Ali Siahkoobi², Mathias Louboutin³ and Felix J. Herrmann¹

¹ Computational Sciences and Engineering, Georgia Institute of Technology, , Atlanta, USA

² Department of Computational Applied Mathematics and Operations Research, Rice University, , Houston, USA

³ Senior Solution Architect, DevitoCodes Ltd, , London, UK

E-mail: rorozco@gatech.edu

Abstract. Due to their uncertainty quantification, Bayesian solutions to inverse problems are the framework of choice in applications that are risk averse. These benefits come at the cost of computations that are in general, intractable. New advances in machine learning and variational inference (VI) have lowered the computational barrier by learning from examples. Two VI paradigms have emerged that represent different tradeoffs: amortized and non-amortized. Amortized VI can produce fast results but due to generalizing to many observed datasets it produces suboptimal inference results. Non-amortized VI is slower at inference but finds better posterior approximations since it is specialized towards a single observed dataset. Current amortized VI techniques run into a sub-optimality wall that can not be improved without more expressive neural networks or extra training data. We present a solution that enables iterative improvement of amortized posteriors that uses the same networks architectures and training data. The benefits of our method requires extra computations but these remain frugal since they are based on physics-hybrid methods and summary statistics. Importantly, these computations remain mostly offline thus our method maintains cheap and reusable online evaluation while bridging the approximation gap these two paradigms. We denote our proposed method **ASPIRE** - **A**mortized posteriors with **S**ummaries that are **P**hysics-based and **I**teratively **R**efined. We first validate our method on a stylized problem with a known posterior then demonstrate its practical use on a high-dimensional and nonlinear transcranial medical imaging problem with ultrasound. Compared with the baseline and previous methods from the literature our method stands out as a computationally efficient and high-fidelity method for posterior inference.

1. Introduction

Inverse problems are fundamental to numerous scientific and engineering fields, wherein one seeks to infer causative factors from observable effects. The central challenge in inverse problems is that they are often ill-posed; the solutions may not exist, be non-unique, or depend discontinuously on the data. This ill-posedness demands

sophisticated mathematical techniques to ensure stable solutions and to explore the family of solutions that can explain the data. The example we treat practically involves challenging medical imaging, where internal structures of the human body (the brain) are inferred from ultrasound measurements through the skull seen in Figure 1. The importance of fast and reliable solutions in this application cannot be overstated as they directly influence possibly life saving diagnostic decisions.

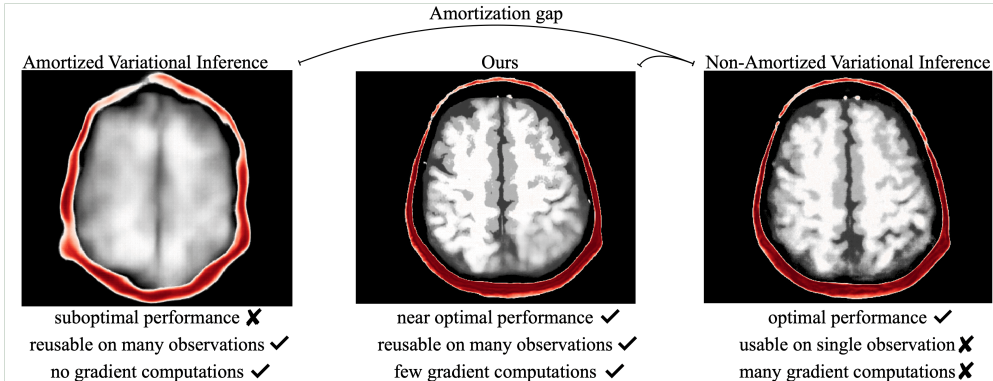


Figure 1: Our algorithm ASPIRE is a middle ground between amortized and non-amortized variational inference.

1.1. Bayesian inverse problems

In this work, we tackle inverse problems that are solutions of the forward problem:

$$\mathbf{y} = \mathcal{G}(\mathcal{F}(\mathbf{x}), \varepsilon) \quad \varepsilon \sim p(\varepsilon). \quad (1)$$

The goal of this inverse problem is to form an image of unknown parameter \mathbf{x} by indirectly observing them through a forward operator \mathcal{F} and noise operator \mathcal{G} , parameterized by the noise instance ε .

In the case of noisy observations and ill-posed forward operators [1], a single deterministic solution to the inverse problem fails to characterize the full space of possible solutions. Bayesian inverse problem solutions [2], on the other hand, offer a more complete characterization of the solution space by adhering to a probabilistic framework. Here the goal is to find a statistical distribution for the parameters that explains the data. The goal is to sample from the conditional distribution $p(\mathbf{x}|\mathbf{y})$, the so-called posterior distribution. This distribution is given by Bayes’ rule

$$p(\mathbf{x} | \mathbf{y}) \propto p(\mathbf{y} | \mathbf{x})p(\mathbf{x}).$$

In words, Bayes’ rule states that a Bayesian solution is formed by updating our prior beliefs of the unknown parameter (prior $p(\mathbf{x})$) with new information given by the observation \mathbf{y} , expressed by the data likelihood, $p(\mathbf{y} | \mathbf{x})$. This likelihood, $p(\mathbf{y} | \mathbf{x})$, encodes our domain knowledge in the form of the forward operator \mathcal{F} and the noise process \mathcal{G} , $p(\varepsilon)$. Thus, posterior samples are the “parameters that are likely under the prior and also likely under the data likelihood—i.e. they explain the observed data”.

Exact posterior inference—i.e., calculating samples from the posterior distribution or its statistics (mean, (co)variance or higher order moments), is in general computationally intractable [3]. The intractable nature of posterior sampling arises from: the curse of dimensionality when dealing with high-dimensional parameters, the expense of forward operator evaluation related to the data likelihood, and multimodality of the distribution, etc. [4]. For specific cases, such as linear forward operators and Gaussian or conjugate priors, the posterior distribution has an analytical form. For example, linear operators, Gaussian noise, and Gaussian priors lead to Gaussian posteriors with known means and covariances [5]. But in many real-world applications, the forward operator is expensive and/or nonlinear and there does not exist a known prior. In these cases, more advanced methods are required for posterior inference. These advanced methods can be divided into two types: the first type of methods are sample based. These include Markov-chain Monte Carlo (MCMC) and its various counterparts [6–8]. On the other hand, there are optimization based methods, such as expectation maximization [9], the Laplace approximation [10], and variational inference (VI) [11]. Here, we consider VI because it can naturally exploit the ability of deep neural networks to learn high dimensional distributions.

1.2. Posterior sampling with variational inference

The technique of VI optimizes an approximate distribution, $p_\theta(\mathbf{x} \mid \mathbf{y})$, $\theta \in \Theta$. The parameters of these distributions are chosen to match the unknown target distribution $p(\mathbf{x} \mid \mathbf{y})$. Due to its connection with maximum likelihood methods [5], and its relatively easy to optimize objective, the mismatch between the approximate and target distribution is typically measured by the Kullback-Leibler (KL) divergence [12]. Because this divergence metric is non-symmetric, it allows for two complementary VI formulations, namely non-amortized VI, which uses the backward KL divergence $\mathbb{KL}(p_\theta(\mathbf{x} \mid \mathbf{y}) \parallel p(\mathbf{x} \mid \mathbf{y}))$ and amortized VI, which involves the forward KL divergence $\mathbb{KL}(p(\mathbf{x} \mid \mathbf{y}) \parallel p_\theta(\mathbf{x} \mid \mathbf{y}))$ [13]. These two formulations have different requirements, costs, and benefits, which we will discuss. Firstly, we will describe the most commonly implemented form: non-amortized VI.

1.3. Non-amortized variational inference

Because the backward KL divergence entails evaluation of the log-likelihood conditioned on a single observation, \mathbf{y}^{obs} , its minimization requires knowledge of the forward operator \mathcal{F} and its gradient. The inference is non-amortized since it is carried out with respect to a single observation. To understand these statements, let us consider the case where the noise is Gaussian with standard deviation σ for which the log-likelihood can be written out explicitly, yielding

$$\begin{aligned} \underset{\theta}{\text{minimize}} \quad & \mathbb{KL}(p_\theta(\mathbf{x} \mid \mathbf{y}^{\text{obs}}) \parallel p(\mathbf{x} \mid \mathbf{y}^{\text{obs}})) \\ & = \mathbb{E}_{p_\theta(\mathbf{x} \mid \mathbf{y}^{\text{obs}})} \left[-\log p(\mathbf{x} \mid \mathbf{y}^{\text{obs}}) + p_\theta(\mathbf{x} \mid \mathbf{y}^{\text{obs}}) \right] \\ & = \mathbb{E}_{p_\theta(\mathbf{x} \mid \mathbf{y}^{\text{obs}})} \left[\frac{1}{2\sigma^2} \|\mathcal{F}(\mathbf{x}) - \mathbf{y}^{\text{obs}}\|_2^2 - \log p(\mathbf{x}) + p_\theta(\mathbf{x} \mid \mathbf{y}^{\text{obs}}) \right]. \end{aligned}$$

From these expressions, we first note that the optimization is indeed performed for a single observation, \mathbf{y}^{obs} . This implies that when inference results are desired for a different observation, the optimization must be repeated, which may be an expensive

proposition in situations where \mathcal{F} and its gradient are expensive to evaluate. For instance, when \mathcal{F} and its gradient require the solution of a partial differential equations (PDE) over a high-dimensional parameter space, their repeated evaluation as part of gradient descent often becomes the most expensive computation when minimizing the backward KL divergence. Finally, minimization of the backward KL divergence also requires evaluation of the prior, $p(\mathbf{x})$, and its gradient. This imposes a difficulty because, in many cases, this prior is not known analytically and must be approximated [14, 15].

There are a variety of implementations of non-amortized posterior inference, including those based on Langevin dynamics [7, 16] and those that make use of normalizing flows [17]. Other examples include methods based on the Stein discrepancy [18, 19] and randomize-then-optimization methods [20, 21]. While these non-amortized inference techniques have shown promise, their online application can be rendered ineffective when applications call for a rapid time-to-solution as may be the case in medical imaging. We will address this situation by presenting an inference technique where most of the computational costs are incurred off-line, so the inference is fast for different observations.

1.4. Amortized variational inference

Guiding distributional optimization with the forward KL divergence as a mismatch metric between the target distribution and the approximate distribution leads to a formulation called amortized VI. To arrive at this formulation, let us first write out the expression for the forward KL divergence:

$$\underset{\theta}{\text{minimize}} \mathbb{KL}(p(\mathbf{x} | \mathbf{y}) || p_{\theta}(\mathbf{x} | \mathbf{y})) = \mathbb{E}_{p(\mathbf{x}|\mathbf{y})} \left[-\log p_{\theta}(\mathbf{x} | \mathbf{y}) + p(\mathbf{x} | \mathbf{y}) \right]$$

and quickly note that evaluating this expression depends on having access to samples from the ground-truth posterior distribution $p(\mathbf{x} | \mathbf{y})$. As these posterior samples are typically not available, we marginalize over the distribution of observations instead—i.e., we have

$$\begin{aligned} \underset{\theta}{\text{minimize}} \mathbb{E}_{p(\mathbf{y})} \left[\mathbb{KL}(p(\mathbf{x} | \mathbf{y}) || p_{\theta}(\mathbf{x} | \mathbf{y})) \right] &= \mathbb{E}_{p(\mathbf{y})} \left[\mathbb{E}_{p(\mathbf{x}|\mathbf{y})} \left[-\log p_{\theta}(\mathbf{x} | \mathbf{y}) + p(\mathbf{x} | \mathbf{y}) \right] \right] \\ &= \mathbb{E}_{p(\mathbf{x},\mathbf{y})} \left[-\log p_{\theta}(\mathbf{x} | \mathbf{y}) + p(\mathbf{x} | \mathbf{y}) \right] \\ &= \mathbb{E}_{p(\mathbf{x},\mathbf{y})} \left[-\log p_{\theta}(\mathbf{x} | \mathbf{y}) \right]. \end{aligned} \tag{2}$$

To arrive at the final expression, we made use of the law of total probability and the fact that the optimization is only over parameters θ . See also [13]. From this final expression, the requirements of training amortized VI become clear: we need samples of the joint distribution $\mathbf{x}, \mathbf{y} \sim p(\mathbf{x}, \mathbf{y})$ and a parametric conditional density estimator. In this work, we obtain samples of the joint distribution using a simulation-based inference framework [22], and train a generative neural network as a conditional density estimator [23] for the posterior.

Amortized VI is so-called “amortized” because its strength lies in its reusability. Once optimized during off-line training, the approximation is not exclusive to a single observation but rather can be applied across numerous observations. This means that the computational expenses involved in the initial optimization phase are effectively “spread out” over multiple inference tasks, making the inference for any new observation significantly cheaper. As we will see in the methods section, this “spread out” practically refers to learning inference tasks over a set of training examples. By learning from examples, the method can remember important features that can be reused at inference time for many unseen observations. Due to this phenomenon, this formulation is sometimes called *inference with memory* while non-amortized inference is called *memory-less inference* [24]. Table 1 summarizes the main requirements and benefits of amortized approaches compared to non-amortized ones.

Table 1: Comparison requirements and benefits of Amortized posterior versus Non-amortized posterior inference

	Amortized posterior inference	Non-amortized posterior inference
Reusable on many observations	Yes	No
Forward operator	Only evaluations	Evaluations and gradients
Needs prior	Only samples	Density calculations

Because non-amortized inference focuses on one single observation, its inference typically outperforms amortized inference [13]. Unfortunately, this improvement often comes at the expense of prohibitively high computational costs at inference time, rendering non-amortized inference impractical in situations where fast turn-around times are needed, such as in many medical imaging fields [25]. Amortized VI methods, on the other hand, while fast [22] at inference may suffer from the so-called amortization gap, a phenomenon that has been studied theoretically [26] and confirmed empirically from comparisons between amortized and non-amortized VI [13, 27, 28]. In that sense, there is a trade-off between runtime and quality at inference time. One either spends more on computations at inference time, or one accepts inferior inference quality in situations where fast turn-around times are essential. While trading quality for speed may be acceptable in some situations, it becomes problematic in circumstances where amortized VI produces unacceptable results, e.g., in cases where the inference problem is high dimensional and complicated by nonlinear forward operators. Currently, the following remedies exist: (1) increase the expressiveness of the parametric family used to approximate the posterior [29] or (2) add more samples to the training set [30]. In this work, we will explore a third complementary option to narrow the amortization gap. To this end, we propose an iterative amortized inference approach during which physics-based summary statistics are refined in tandem with neural posterior estimators thus bootstrapping the quality of the approximated posterior. We call this approach: **ASPIRE** - **A**mortized posteriors with **S**ummaries that are **P**hysics-based and **I**teratively **R**Efined. To motivate this approach, we will first explore the implementation of amortized posterior inference via neural density estimation, followed by physics-based gradient summary statistics, and their iterative refinement.

2. Contributions

1. Motivated by score-based, maximally informative summary statistics we introduce the ASPIRE algorithm, which iteratively refines amortized posterior inference while maintaining low online costs.
2. Evaluation of our method on a stylized problem to ensure that the approximate posterior accurately samples the ground-truth posterior.
3. Evaluation of our method’s performance on a realistic and challenging transcranial medical imaging inverse problem with ultrasound, focusing on the accuracy of the posterior mean and the effectiveness of our uncertainty in predicting reconstruction errors.
4. Introduction of a novel non-amortized inference method to serve as a “gold standard”.
5. Qualitative and quantitative comparisons against a current literature baseline and our “gold standard” non-amortized inference method. To accelerate the development of inference techniques for transcranial medical imaging [31], we introduce benchmarks with accompanying datasets and code.
6. Cost-benefit analysis of the computational costs associated with offline training versus the rapid online capabilities of the amortized method.

3. Method

To close the amortization gap, we describe an iterative approach to posterior inference where learned physics-based summary statistics are refined with Conditional Normalizing Flows (CNFs). VI with CNFs is reviewed first. Its improvement with learned physics-based summary statistics is discussed next, including addition of the crucial refinement step.

3.1. Amortized variational inference with conditional normalizing flows

While our method can, in principle, be applied to any generative model (GAN, diffusion, VAE), we focus on normalizing flows [32]. Thanks to their simple maximum-likelihood training objective, low training memory requirements [33], and fast sampling, CNFs have become one of the generative methods of choice when inverse problems are concerned. CNFs learn to sample from a target density by learning invertible transformations from the data distribution to the standard Normal distribution. By taking advantage of the change of variables formula [34], CNFs can be trained with a relatively simple objective:

$$\hat{\boldsymbol{\theta}} = \operatorname{argmin}_{\boldsymbol{\theta}} \frac{1}{N} \sum_{n=0}^N \left(\frac{1}{2} \|f_{\boldsymbol{\theta}}(\mathbf{x}^{(n)}; \mathbf{y}^{(n)})\|_2^2 - \log |\det \mathbf{J}_{f_{\boldsymbol{\theta}}}| \right), \quad (3)$$

where the neural network’s Jacobian, $\mathbf{J}_{f_{\boldsymbol{\theta}}}$, is calculated with respect to the target variable \mathbf{x} . Please refer to [13], for a derivation on the above expression from the generic amortized posterior objective in Equation 2. The training pairs, collected in $\mathcal{D} = \{(\mathbf{x}^{(n)}, \mathbf{y}^{(n)})\}_{n=0}^N$, are generated by sampling from the prior, $\{\mathbf{x}^{(n)}\}_{n=0}^N \sim p(\mathbf{x})$, followed by a forward simulation applying Equation 1. After the optimization is completed, the CNF with optimized weights, $\hat{\boldsymbol{\theta}}$, can be used to sample from the approximate posterior $p_{\hat{\boldsymbol{\theta}}}(\mathbf{x} \mid \mathbf{y} = \mathbf{y}^{\text{obs}})$ by sampling Gaussian noise and passing it through the inverse network that is conditioned on an observation \mathbf{y}^{obs} .

$$\mathbf{x} = f_{\hat{\theta}}^{-1}(\mathbf{z}; \mathbf{y}^{\text{obs}}) \text{ where } \mathbf{z} \sim \mathcal{N}(0, I). \quad (4)$$

Contrary to non-amortized VI, the above posterior sample generation holds for any observation, \mathbf{y}^{obs} , as long as the observations remain close—i.e., the \mathbf{y}^{obs} are produced by applying Equation 1 to samples of the prior, $\mathbf{x} \sim p(\mathbf{x})$. However, the quality of the posterior approximation, and therefore the quality of its samples— $\mathbf{x} \sim p_{\hat{\theta}}(\mathbf{x} | \mathbf{y} = \mathbf{y}^{\text{obs}})$, depends on the complexity of the posterior that is being approximated. This in turn depends on the complexity of prior samples and the likelihood. To account for realistic situations where both the prior and likelihood are complicated, CNFs demand increases in the size of the training set and the expressive power of the density estimator $f_{\theta}(\cdot)$, a requirement we like to avoid. For this reason, we will introduce the concept of *summary statistics* that allows us to improve the quality of the posterior approximation in these situations.

3.2. Score-based summary statistics

While CNFs are in principle capable of capturing complex data-to-image space mappings, amortization can be challenging to achieve in situations where the mapping is complex, or the observed data are heterogeneous—i.e., the observed data differ in dimension and/or source-receiver acquisition geometry. To overcome these challenges, statisticians introduced so-called *summary statistic*. These often hand-derived summary statistics are designed to capture the main features in the data, reduce and homogenize its dimensionality, while posterior distributions remain informed [23]. For compressed posterior distributions to remain informed, it is essential in all approaches that the conditioning by the summary statistic, denoted by $\bar{\mathbf{y}}$, minimally changes the original conditional distribution—i.e., we have

$$p(\mathbf{x}|\bar{\mathbf{y}}) \approx p(\mathbf{x}|\mathbf{y}).$$

When this approximate equality holds exactly, the summary statistic is known to be a sufficient summary statistic. Since equality can not always be met, there also exists the notion of being close to sufficient. To be more specific, a summary statistic remains maximally informative [35] with respect to a set of summary statistics $\mathbf{y}' \in \mathbf{Y}$ when some distance measure between the summarized and original posterior distributions is minimized. For a distance measure given by the KL divergence, this amounts to finding the minimum of the following objective:

$$\bar{\mathbf{y}} = \underset{\mathbf{y}' \in \mathbf{Y}}{\operatorname{argmin}} \mathbb{KL}(p(\mathbf{x} | \mathbf{y}') || p(\mathbf{x} | \mathbf{y})).$$

Alternatively, one can also measure the informativeness of a certain summary statistic by its Fischer information [36], which corresponds to the expected variance of the score function given by the gradient of the natural logarithm of the likelihood. Based on this argument, [37] proposed the gradient of the log-likelihood $\nabla_{\mathbf{x}} \log p(\mathbf{y} | \mathbf{x})$ as a maximally informative summary statistic. It can be shown that under certain assumptions the information inequality is saturated by the gradient of the log-likelihood, in other words that no other summary statistic can have more Fischer information [37]. The gradient of the log-likelihood is an attractive summary statistic because it

(the score function) allows for the inclusion of knowledge on the forward operator, \mathcal{F} , and its Jacobian, $\nabla\mathcal{F}$. For instance, if the noise is Gaussian and the noise operator \mathcal{G} is additive then the summary statistic is given by the action of the adjoint of the Jacobian, $\nabla\mathcal{F}^\top[\mathbf{x}_0]$ evaluated at \mathbf{x}_0 , on the residual. In that case, we can write

$$\bar{\mathbf{y}} = \nabla_{\mathbf{x}} \log p(\mathbf{y} | \mathbf{x}) \Big|_{\mathbf{x}_0} = \nabla\mathcal{F}^\top[\mathbf{x}_0](\mathcal{F}(\mathbf{x}_0) - \mathbf{y}). \quad (5)$$

To train a CNF with this gradient summary statistic, the objective of Equation 3 is minimized on a new training set obtained by applying Equation 5 to the observed datasets collected in \mathcal{D} , yielding $\mathcal{D}_0 = \{\mathbf{x}^{(n)}, \bar{\mathbf{y}}_0^{(n)}\}_{n=0}^N$. The subscript 0 was added in our notation to indicate that each single summary statistic, $\bar{\mathbf{y}}_0^{(n)}$, derives from the evaluation of the gradient at $\mathbf{x}_0^{(n)}$, a point which is henceforth referred to as a fiducial point. This fiducial point represents a trusted guess of the unknown parameter.

The quality of gradient summary statistics is contingent on two key factors, namely the quality of the assumed likelihood and the quality of the fiducial points. The quality of the former depends on choices for the noise distribution and the forward operator, \mathcal{F} . When misspecified, or poorly calibrated, these choices may affect the quality of the summary statistic. We assume in this work that the forward problem and noise model are well specified. The second factor that determines the quality concerns choices for the fiducial points themselves. Because the fiducial point is used to calculate the score function then its choice correlates with the information content of the resulting score. Thus, the choice for these fiducial points determines the quality of the summary statistic, which in turn determines the quality of the posterior inference itself. As shown by [37], fiducial points that stay close to the maximum likelihood:

$$\mathbf{x}_{ML} = \underset{\mathbf{x}}{\operatorname{argmax}} p(\mathbf{y} | \mathbf{x})$$

lead to score-based summary statistics that are maximally informative with respect to the Fisher information. However, in the common situation where the fiducial points are not close to the maximum likelihood this property may potentially no longer hold, rendering score-based summary statistics less informative. As in many practical situations, we unfortunately do not always have access to high-quality fiducial points, a situation we will remedy in the next section where data-driven learning will be combined with score-based summary.

Before introducing a novel iterative approach to render fiducial points more informative, note that the assumed likelihood in Equation 5 need not be the actual likelihood $p(\mathbf{y} | \mathbf{x})$. Indeed, as discussed by [38], this summary statistic is still applicable in methods that are likelihood-free since you only need an assumed likelihood to be reasonably close to the true likelihood, or learned likelihoods [39] derived from samples of the likelihood.

3.3. Refining summary statistics

Notwithstanding the fact that score-based summary statistics represent a natural approach to inference problems that involve well-understood physics, reliance on good fiducial points—i.e., points that are close to their respective maximum likelihoods, remains problematic especially in situations where inference problems are ill-posed or reliant on good starting parameters to succeed. Instead of performing expensive, and

potentially local-minima prone [40], Gauss-Newton updates to bring the fiducial points closer to the maximum likelihood points, as suggested by [38], we propose an iterative scheme during which CNFs are trained then sampled to estimate improved fiducial points. The iterations, outlined in Figure 2, proceed as follows: given the current iterate for the fiducial points, this would be $\{\mathbf{x}_0^{(n)}\}_{n=0}^N$ at the first iteration, score-based summary statistics are computed with Equation 5 and a CNF is trained on \mathcal{D}_j ($j = 0$, for the first iteration) by minimizing Equation 3. This minimization produces optimized CNF weights, $\hat{\theta}_j$, which are used to draw multiple samples from the posterior, via Equation 4, for each simulated observation in $\{\bar{\mathbf{y}}_j^{(n)}\}_{n=0}^N$. Next, these posterior samples are averaged to approximate the expectation, $\{\mathbf{x}_{j+1}^{(n)} = \mathbb{E}[p_{\hat{\theta}_j}(\mathbf{x} | \bar{\mathbf{y}}_j^{(n)})]\}_{n=0}^N$, computed for each score-based summary statistic, separately. This averaging, which corresponds to approximating the posterior mean for each $\{\bar{\mathbf{y}}_j^{(n)}\}_{n=0}^N$, produces the next, and arguably improved set of fiducial points, $\{\mathbf{x}_{j+1}^{(n)}\}_{n=0}^N$. This process is repeated J times. As long as the new set of fiducial points moves closer to the maximum likelihood points, the quality of the score-based summary statistic can be expected to improve. These improvements in turn produces better posterior inferences by the CNFs.

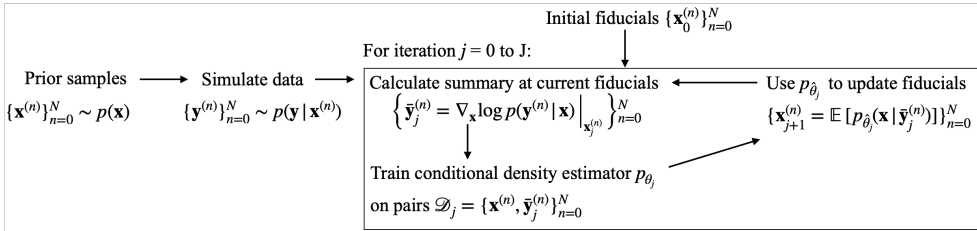


Figure 2: Offline training phase: During training, our proposed algorithm refines the fiducial point used to calculate the summary statistics. Importantly, this refinement is done in an amortized manner over a training dataset.

The above iterative refinement scheme hinges on the assumption that the fiducial points improve—i.e., they are indeed closer to the maximum likelihood points. We argue that improvements are to be expected for a few reasons. First, the gradient of the log-likelihood that defines our summary statistic engenders the first iteration of gradient descent, which under certain conditions is known to move initial fiducial points closer to the maximum-likelihood points [41]. [38] used the same argument by suggesting that a limited number of Gauss-Newton updates improves the informativeness of these refined fiducial points. Second, we propose to update the fiducials with the average samples from the posterior for each observation. This average, known as the posterior mean, is unbiased and contains information on the prior. To add some rigor, we summarize our claim with the following lemma:

Lemma 3.1. *If the score $\bar{\mathbf{y}}_0$ is calculated at a fiducial \mathbf{x}_0 that is inside the basin of attraction of the maximum likelihood \mathbf{x}_{ML} and the conditional density estimator $p_{\hat{\theta}_0}$ is trained on dataset \mathcal{D}_0 to convergence then \mathbf{x}_1 defined by the mean of the conditional density estimator samples will be closer to the maximum-likelihood \mathbf{x}_{ML} :*

$$\|\mathbf{x}_1 - \mathbf{x}_{ML}\|_2 < \|\mathbf{x}_0 - \mathbf{x}_{ML}\|_2 \quad \text{where } \mathbf{x}_1 = \mathbb{E}_{\mathbf{x}}[p_{\hat{\theta}_0}(\mathbf{x} | \bar{\mathbf{y}}_0)].$$

Informally, Lemma 3.1 derives from the observation that the conditional mean of

the posterior distribution is the estimator that minimizes the mean-squared error with respect to the ground truth, \mathbf{x}^* [42]. Since the \mathbf{x}^* 's are also maximally likely, then CNF updates that bring the \mathbf{x}_0 's closer to \mathbf{x}^* will also make them closer to maximum-likelihood. If Lemma 3.1 holds, initial (potentially poor) summary statistics computed for the fiducial points, $\{\mathbf{x}_0^{(n)}\}_{n=0}^N$, can be improved by training a CNF to generate new fiducial points, $\{\mathbf{x}_1^{(n)}\}_{n=0}^N$. Since these new fiducial points are closer to their corresponding maximum likelihood then the new summary statistics will be more informative, improving inference during the next iteration where the CNF is trained on these improved summary statistics.

After training is completed, we obtain J trained CNFs, each with their own set of optimized weights, $\hat{\theta}_j = 0 \dots J - 1$. Because these networks are trained on $\{(\mathbf{x}_j^{(n)}, \bar{\mathbf{y}}_j^{(n)})\}_{n=0}^N$ for $j = 0 \dots J - 1$, these networks have been amortized to perform J refinements, given a new unseen observation, \mathbf{y}^{obs} . A schematic for the online inference phase is included in Figure 3. Note that each refinement incurs the cost of a gradient calculation. In practice, $J = 3$ to 4 refinements are often adequate resulting in a total online computational cost that is significantly lower than non-amortized inference, which can result in 10000's of gradients [43].

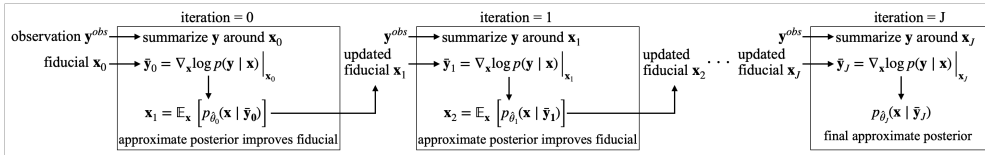


Figure 3: Online inference phase: our algorithm refines the fiducial used to calculate the summary statistics. During inference, it maintains the ability to amortize to many observations and has low cost since J is typically a low number (3-4).

In summary, by pairing the theory of [37] with Lemma 3.1, we arrived at a formulation where the refined fiducial points yield improved summary statistics and refine amortized VI at limited additional online computational costs. To verify this claim, we will first evaluate our method on a stylized example for which the analytical posterior is known. This example will show that the improvements thanks to refined summary statistics indeed lead to converge to the correct posterior distribution. To demonstrate our amortized VI in a more practical setting, we will also evaluate its performance on a realistic ultrasound transcranial medical imaging problem. Finally, although the above lemma assumes that the fiducial points reside in the correct basin of attraction, we believe that the prior information contained in the paired datasets \mathcal{D}_j , $j = 0 \dots J - 1$ may mitigate the effect of local minima. Indeed, our initial results in the nonlinear medical imaging example start from a poor fiducial suggesting this might be possible.

3.4. Stylized example

To build trust in our method, we first demonstrate it improves the quality of the posterior approximation by testing on an inverse problem with a known posterior distribution. One such inverse problem is the linear Gaussian inverse problem where: the forward operator \mathcal{F} is a known matrix $\mathbb{R}^{m \times n}$, the prior and noise comes from Gaussian distributions with known means and covariances. We chose the unknown

parameter vector to have size $n = 16$ and the data as size $m = 80$. Given these settings, it is possible to calculate samples from the analytical posterior distribution [5]. We use samples from the analytical posterior distribution to compare against our posterior sampling results with ASPIRE.

We train our method using $N = 1000$ samples from the Gaussian prior and use the forward operator to form training pairs. Since the forward operator is linear, the score-based summary statistic is calculated from the transposed operator. After training, we evaluate our method on an unseen observation, \mathbf{y}^{obs} , simulated from a known ground-truth parameter \mathbf{x}^* . We first observe that after each ASPIRE iteration the posterior mean $\mathbb{E} p_{\hat{\theta}_j}$ (using short hand described in Equation E.1) becomes a better reconstruction of the ground truth \mathbf{x}^* as seen in Figure 4.

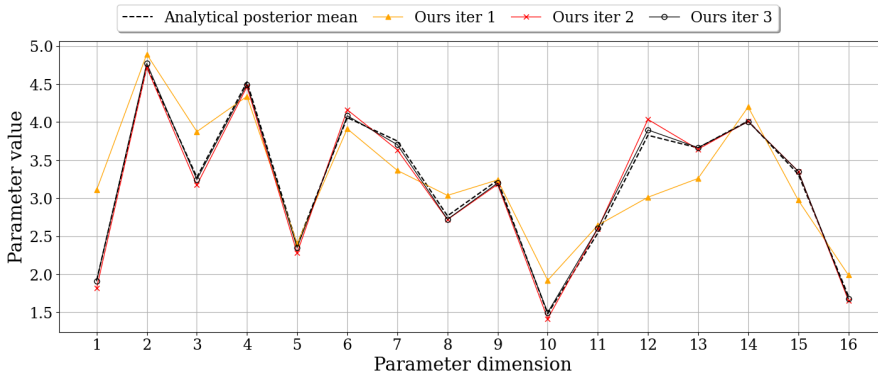


Figure 4: The quality of the proposed amortized posterior approximation improves at each iteration as measured by the estimated posterior mean with respect to the analytically known ground truth posterior mean.

Furthermore, Figure 5 shows the empirical covariance derived from our method’s posterior samples, compared to the analytically calculated covariance matrix. It is clear that each iteration improves the approximation of the estimated covariance and it is almost exactly correct at the third iteration, $J = 3$. While this stylized example confirms that amortized inference with ASPIRE in principle be feasible, the real challenge is to apply this concept to medical ultrasound where problems are high dimensional and forward modeling computationally expensive to evaluate.

4. Medical wave-based imaging

Transcranial Ultrasound Computed Tomography (TUCT) is a non-ionizing, non-radiative imaging modality that creates images of brain tissue from measurements of impinging ultrasound waves due to contrast in tissue acoustic properties. Unlike other ultrasound imaging targets, like breast imaging [44, 45], TUCT faces the challenge of high acoustic contrast in the cranial bone, leading to scattering unsuitable for traditional traveltime tomography methods [46]. Tomographic methods require high frequencies for higher resolution imaging, but attenuation through the skull is exacerbated at higher frequencies thus preventing high-resolution imaging when relying on traveltime methods. This challenge has hindered ultrasound’s application to brain imaging until

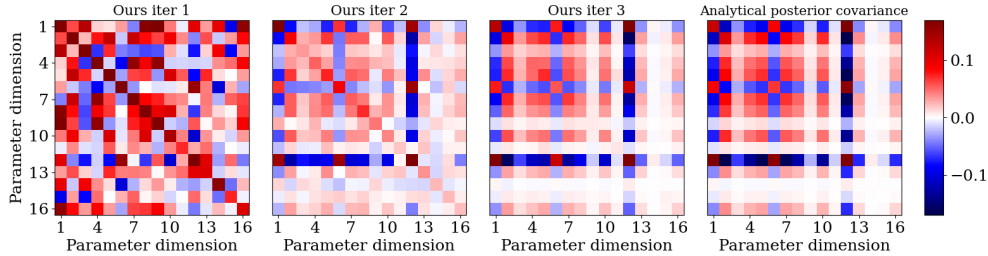


Figure 5: Comparison of full covariance matrix from our method as compared to the analytical ground truth posterior covariance. After three iterations of our method, the estimated posterior covariance is close to the ground truth covariance.

recent developments when [47] identified that similar challenges exist in transcranial ultrasound imaging as with sub-salt imaging used by exploration seismology. The main reason seismic techniques are capable of imaging through high-acoustic contrast salt is because these sophisticated inversion methods model the full physics of the wave equation to make sense of the scattered waves. Whereas traditional ultrasound only uses arrival times, seismic imaging techniques model all waveforms allowing for higher effective resolutions at lower frequencies that experience less attenuation through the skull. These methods are denoted Full-Waveform Inversion (FWI) since they model and match the full observed waveform, see Figure 6c for an example of the full waveform.

4.1. Medical ultrasound with full-waveform inversion

Since the groundbreaking work of [47], FWI techniques for TUCT are showing promise as a high-resolution imaging modality with potential clinical applications ranging from early hemorrhage diagnosis to tumor imaging [48, 49]. The TUCT inverse problem involves reconstruction of the acoustic velocity, \mathbf{x} , of brain tissue from acoustic data, \mathbf{y} , collected as shown in Figure 6a. In this setup, ultrasound transducers placed around the patient’s head perform multiple experiments, with each involving a tone-burst transmission by one transducer and recording by all others, as simulated in Figure 6c. Experiments proceed by transducers transmitting from different positions until all transducers have transmitted, providing a full coverage from many angles. The forward operator \mathcal{F} that maps the acoustic parameters to the observed data is simulated with the numerical solution of the second-order wave equation with varying acoustic velocity in two space dimensions:

$$\frac{1}{c(x, y)^2} \frac{\partial^2}{\partial t^2} u(x, y, t) - \nabla^2 u(x, y, t) = q_s(x, y, t). \quad (6)$$

where the acoustic velocity $c(x, y)$ is parameterized by a gridded array of values in the unknown vector \mathbf{x} and the transducers are modeled by N_s different source terms $\{q_s(x, y, t)\}_{s=0}^{s=N_s}$. Although the forward operator \mathcal{F} is technically defined for each source as $\mathcal{F}(\mathbf{x}; q_s)$, for simplicity, we denote it as $\mathcal{F}(\mathbf{x})$, representing the collection of PDE solutions for all transducer sources that contribute to all the observations collected in \mathbf{y} and the restriction of the solution wavefields to receiver positions. Given the set of observations, traditional FWI workflows setup the variational problem

$$\underset{\mathbf{x}}{\text{minimize}} \|\mathcal{F}(\mathbf{x}) - \mathbf{y}\|_2^2$$

and minimize this data-misfit objective with stochastic gradient descent by using randomized subsets of the sources to calculate the gradient of each descent step beginning from the starting parameter vector, \mathbf{x}_0 . This, of course, assumes access to an efficient routine for calculating the gradient of \mathcal{F} , which we will discuss further in Section 4.2.3. Under controlled assumptions, such as a good starting parameter \mathbf{x}_0 and calibrated transducers [50], FWI is known to produce high-resolution images [47, 51]. However, clinical adoption of FWI is hampered by the prohibitively long runtime of full physics modeling and the parasitic local minima related to the non-convex optimization [52]. Previous literature has explored the regularization of the FWI optimization with handcrafted priors such as the Total Variation norm [53, 54] and model extensions [40, 55]. Our approach, ASPIRE, addresses these issues by reducing physics computations, giving data-driven regularization of the non-convex optimization, and providing uncertainty-aware solutions crucial for clinical applications by sampling the Bayesian posterior.

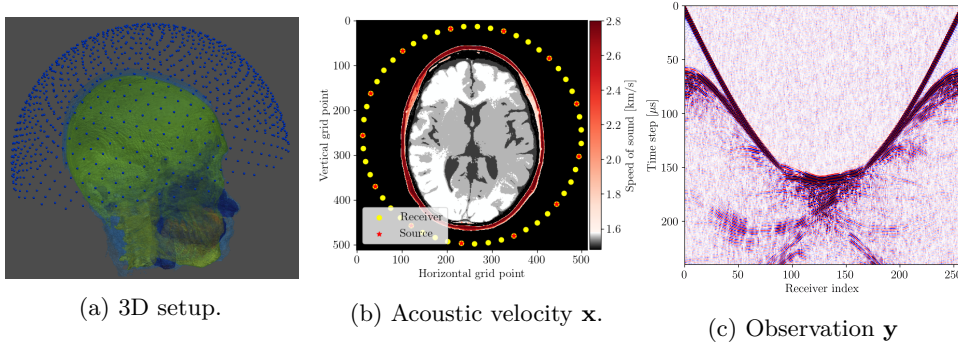


Figure 6: Experimental setup (a) Transcranial ultrasound 3D setup as used in field, blue dots indicate transducers. (b) Transcranial ultrasound 2D synthetic experimental setup used in this work. (c) Simulated waveform from a single source synthetic experiment \mathbf{y} . Each column corresponds to acoustic-pressure amplitudes measured at one transducer for a single experiment.

4.2. Transcranial Ultrasound Computed Tomography with ASPIRE

To abridge, we will use ASPIRE to solve TUCT by generating samples from a realistic brain velocity prior $\mathbf{x} \sim p(\mathbf{x})$, use a wave PDE solver \mathcal{F} to simulate acoustic data \mathbf{y} and use the gradient of the simulator at a fiducial point \mathbf{x}_0 as the score-based summary statistic for training a CNF with Equation 3. Our test results demonstrate that iterative refinement of this summary statistic through ASPIRE significantly enhances the accuracy of the posterior approximations. Now, we detail how each of these experiments and tests are implemented.

4.2.1. Brain prior samples: The first step of implementing ASPIRE concerns obtaining samples from a realistic prior for the target parameter vector $\mathbf{x} \sim p(\mathbf{x})$, in this case, gridded velocity parameters of human brains and skulls. The parameters collected

in the MIDA dataset [56] correspond to a single 3D volume for the acoustic velocity collected from a single subject and will unfortunately not be appropriate to train a neural model that will generalize to other human patients. As far as we know, there is no dataset that includes acoustic velocity collected from many patients, so we made our own dataset based off the multi-subject FASTMRI dataset [57]. This custom dataset, detailed in Section Appendix A, comprises $N=1000$ diverse acoustic velocity parameters collected from different human patients, $\{\mathbf{x}^{(n)}\}_{n=0}^{1000}$. This size of datasets facilitates generalization of the amortized posterior sampler across different datasets collected from unseen patients. The dataset is accessible via the repo ASPIRE.jl.

4.2.2. Wave simulations: Our synthetic TUCT experiment, based on the configuration from [47], models the unknown parameter as discretized acoustic velocity on a 512×512 grid, with a 0.5 [mm] discretization. We modeled transducer sources as point sources with a three-cycle tone-burst signature with central frequency of 400Khz and 240 [microseconds] recording time. The transducers are placed in a circular arrangement around the skull, the setup, with 16 sources and 256 receivers, mimics a 2D slice of the 3D experiment shown in Figure 6b. The forward operator, $\mathcal{F}(\mathbf{x})$, corresponds simulating the forward waveforms and their restriction to the receiver locations. The wave equation and its Jacobian were solved using the open-source software packages Devito and JUDI [58–60], which automatically generate optimized C code and leverage GPU accelerators, thereby facilitating scalability to realistic problem sizes. To simulate noise corruption, we used additive Gaussian noise, ε , with a 35dB Signal-Noise-Ratio, matching lab values [47]. A synthetic observation, $\mathbf{y} = \mathcal{F}(\mathbf{x}) + \varepsilon$, is displayed in Figure 6c.

4.2.3. TUCT summary statistic: The score-based summary statistic $\bar{\mathbf{y}}$, is calculated as in Equation 5, which requires the action of the Jacobian adjoint on the data residual at the fiducial point, \mathbf{x}_0 . For computational efficiency, the adjoint-state method [61, 62] is used. To avoid the inverse crime, the observed data is simulated with finer time discretization and a higher-order spatial finite-difference stencil than those used in the residual calculation and adjoint simulation. Each transducer defines a source term in Equation 6, so we sum the gradient over all 16 sources into the final summary statistic.

4.3. Traditional amortized inference

To illustrate the limitations of amortized VI, we train a CNF on pairs $\{(\mathbf{x}^{(n)}, \mathbf{y}^{(n)})\}_{n=0}^N$ without evoking iterative improvements by ASPIRE. We emphasize that the observations \mathbf{y} are the raw unsummarized waveforms similar to that shown in Figure 6c. Training details are included in Section Appendix C. After training by minimizing Equation 3, the CNF with weights $\hat{\boldsymbol{\theta}}$, provides an amortized approximation of the posterior, $p_{\hat{\boldsymbol{\theta}}} \approx p(\mathbf{x} | \mathbf{y})$, from which we can sample (cf. Equation 4). The results, shown in Figure 7, demonstrate that the samples from $p_{\hat{\boldsymbol{\theta}}}$, for an unseen test observation, \mathbf{y}^{obs} , lack distinct features beyond an unrealistic skull and unresolved internal tissue structure. A comparison of these samples and the posterior mean, $\mathbb{E} p_{\hat{\boldsymbol{\theta}}}$, in Figure 7c with the ground truth, Figure 7d, highlights the poor quality of this approximation. Note, throughout this exposition we calculate the posterior statistics (i.e. mean and standard deviation) over 512 samples, please consult the Section Appendix E for a discussion on this quantity. This experiment underscores the challenge of directly learning the probabilistic inverse mapping from the acoustic data \mathbf{y} to the velocity

parameters, a difficulty previously noted in the literature [63]. This challenge is often referred to as the ‘end-to-end’ problem [64]. We address this problem with the score-based summary statistic employed by ASPIRE.

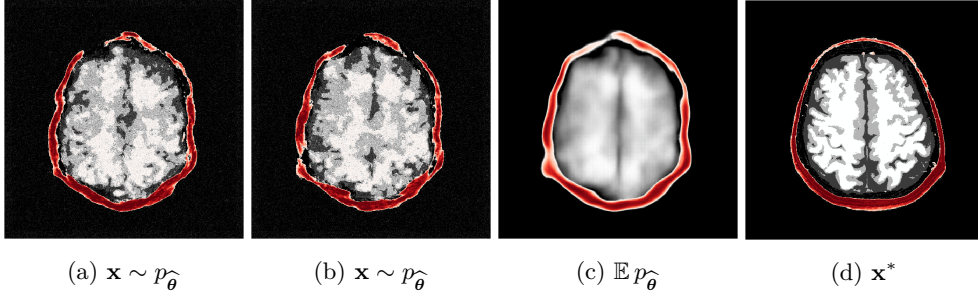


Figure 7: Baseline amortized inference. (a),(b) Posterior samples. (c) Posterior mean. (d* Ground-truth velocity parameters paired to test observation $\mathbf{y}^{\text{obs}} = \mathcal{F}(\mathbf{x}^*) + \varepsilon$. The samples have poor quality since it is difficult to learn the direct mapping from acoustic waveforms to the unknown parameter.

4.4. Amortized inference with score-based summary statistics

To overcome the end-to-end inference problem, we apply one iteration of ASPIRE by training a CNF on pairs, $\mathcal{D}_0 = \{(\mathbf{x}^{(n)}, \bar{\mathbf{y}}_0^{(n)})\}_{n=0}^N$, where the $\bar{\mathbf{y}}_0^{(n)}$ ’s represent the score-based summary statistics at the fiducial points, $\mathbf{x}_0^{(n)}$, taken to be the uniform water velocity for all samples. An example of this initial summary statistic is shown in Figure 8a. While the outer edge of the skull is reasonably well delineated, the inner edge of the skull is still poorly resolved and details inside the skull are mostly absent. However, the inference based on these initial summary statistics, shown in Figure 9c, present a significant improvement over the baseline (cf. Figure 7c), despite the presence of strong imaging artifacts in the summary statistics. The improvements concern the skull’s structure in particular, although details within the skull remain elusive due to the summary statistic’s limited information. To enhance fidelity further, ASPIRE 2 (shorthand for ASPIRE at iteration $J = 2$) is applied by recalculating the score at the new posterior mean estimate for each training sample. Given these new training pairs, the next CNF is trained. While posterior sampling is efficient with CNFs (using Equation 4), recalculation of the score for each sample is computationally intensive, a topic we address in Section 6.6.

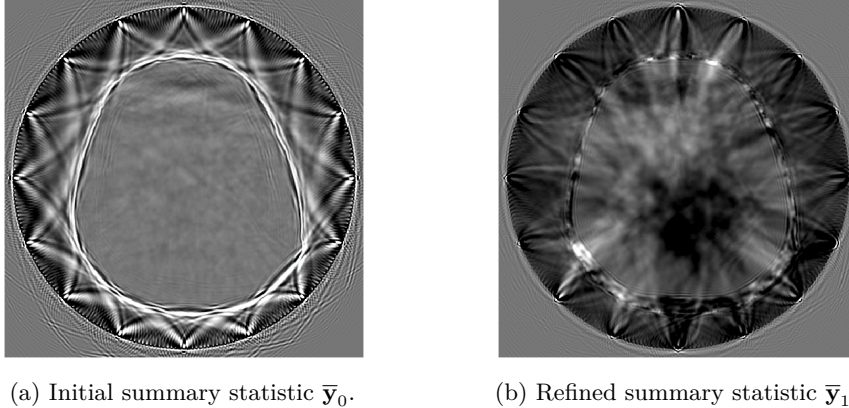


Figure 8: Score-based summary statistics (a) First summary statistic calculated at the \mathbf{x}_0 fiducial consisting of constant water velocity. (b) Second summary statistic calculated at the fiducial point, \mathbf{x}_1 , derived from the first CNF posterior mean. Thanks to improved fiducial point, we now can “illuminate” the inside of the skull.

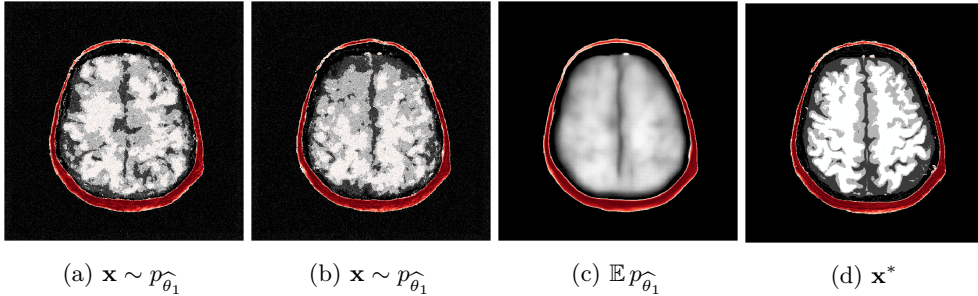
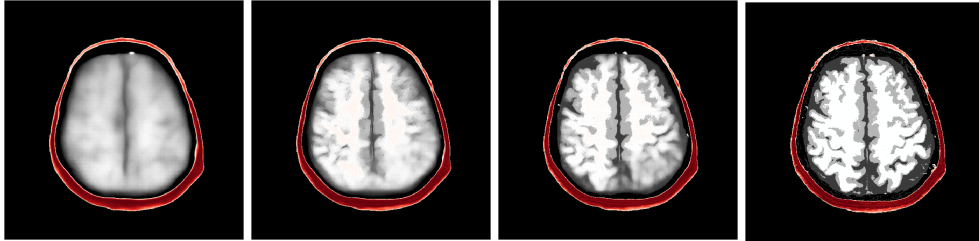


Figure 9: The first iteration of our method learns the mapping from the summarized data $\bar{\mathbf{y}}$ to unknown parameter \mathbf{x} (a),(b) Posterior samples. (c) Posterior mean. (d) Ground-truth velocity parameters. Our method has learned to reconstruct a reasonable estimate of the skull outline by making use of the summary statistic.

4.5. Amortized inference with iterative refinements

After the refinements of ASPIRE 2, significant improvements are evident in the posterior samples, particularly in capturing the structures within the brain tissue itself. The mean of these posterior samples, displayed in Figure 10b, is clearly enhanced in resolution and details. We attribute these enhancements to the increased informativeness of the summary statistic in the second iteration compared to the information yielded by the initial iteration. A detailed inspection of the second summary statistic (shown in Figure 8b) reveals more detail on the internal brain structures. Unlike the first summary statistic (cf. Figure 8a), which primarily delineated the skull, the second iteration’s summary statistic better ‘illuminates’ the softer tissues within the brain, offering a more informative image for the posterior network. Thanks to accounting for the scattering at the skull, the acoustic illumination of the brain is improved

significantly. Accurately resolving the skull structure is an important consideration as noted by [65].



(a) ASPIRE 1 $\mathbb{E}p_{\hat{\theta}_1}$ (b) ASPIRE 2 $\mathbb{E}p_{\hat{\theta}_2}$ (c) ASPIRE 4 $\mathbb{E}p_{\hat{\theta}_4}$ (d) Ground truth \mathbf{x}^*

Figure 10: The posterior approximation improves as measured by the posterior mean quality. (a) Posterior mean from ASPIRE 1 where the observation is preprocessed with the gradient as summary statistic. (b) Posterior mean from ASPIRE 2 where the summary statistic has been refined using the posterior mean from the first iteration. (c) Posterior mean from ASPIRE 4. (d) Ground-truth.

As one can observe from Figure 10, the reconstruction quality improves for increasing number of refinements of ASPIRE. By virtue of the iterative recalculation of the score-based summary statistic, the method is progressively able to discern finer details within the brain albeit the updates become less pronounced as the number of refinements increases. We further illustrate this refinement by plotting posterior samples from all four ASPIRE iterations in Figure D1. Practically, a user of ASPIRE can decide on the number of refinements based on the amount of compute available or by refining until there are diminished returns on enhancements.

4.6. Reconstruction quality

To quantitatively assess enhancements of each ASPIRE iteration, we compare the posterior means with their corresponding ground truths, using a test set comprising 50 unseen observations. By calculating the Root Mean Squared Error (RMSE) for these comparisons, we establish a metric to quantify the improvements across iterations. At each iteration we plot the RMSE for all examples in the test set and plot a box plot. We emphasize that testing on this many samples was only tractable since the posterior sampler is amortized. The trend, as showcased in Figure 11, confirms that on average each iteration reduces the RMSE, indicating an increasingly precise approximation of the true posterior means. We hypothesize that we are observing the effect known as Bayesian contraction [66] since each summary statistic is extracting more information from the observations.

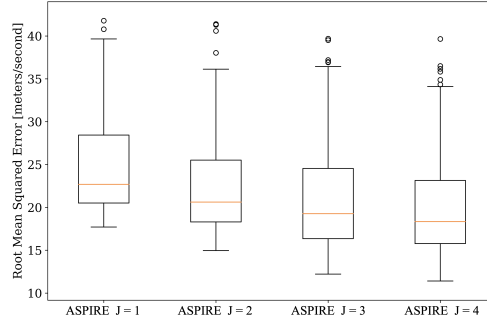


Figure 11: Image quality metric measured on average over 50 sample leave-out test set. The quality of the posterior mean improves after each ASPIRE refinement.

While the reconstructions in Figure 10 clearly improve as the number refinements increases, certain areas remain smooth, especially near the top and lower-right corner. This smoothing effect of the posterior mean is well-known and arises from relative strong variations among the samples in certain areas. Variations between samples are a reflection of inconsistent reconstructions by the posterior samples and correspond to areas of increased uncertainty. This phenomenon is a direct result of treating ultrasound medical imaging as an inference problem that produces posterior distributions instead of a single answer.

5. Uncertainty quantification

Due to the risk of hallucinations, generative AI for imaging inverse problems benefits from uncertainty awareness. Furthermore, an uncertainty-aware approach becomes crucial in medical applications, as underscored by [67]. Fortunately, Bayesian posterior sampling provides a natural sense of uncertainty, reflected in the spread of the samples. ASPIRE is designed with amortized posterior sampling in mind to quickly deliver crucial uncertainty quantification. By providing both the mean and a uncertainty information, our method offers a dual perspective, namely a robust reconstruction of the tissues, complemented by an insight into the statistical variations of each pixel’s value. This dual analysis is particularly valuable in medical diagnostics, where understanding both the image and the associated uncertainty is crucial for decision making.

5.1. Amortized uncertainty quantification

To visualize uncertainty, we calculate uncertainty images by taking the pixel-wise standard deviations $\sqrt{\mathbb{V}}$ as defined in Equation E.2 with 512 posterior samples. Figure 12 shows uncertainty images for four iterations of ASPIRE alongside the error of the posterior mean from the ground truth. From these figures, we make the following qualitative observations: (1) uncertainty images increase in resolution with each ASPIRE refinement (2) refinements increase correlations between the uncertainty and the error. Specifically, the errors concentrate near the top and lower-right of the internal brain tissue. The reason being that high acoustic contrast in these areas is creating multiple reverberations of the wavefield inside the brain impeding accurate imaging, importantly these are areas that are highlighted by the uncertainty.

Correlations between the uncertainty and the error constitute important empirical evidence of the trustworthiness of the uncertainty. To more rigorously quantify this correlation, and quantitatively validate the uncertainty quantification, we study the calibration of our uncertainty in the following section.

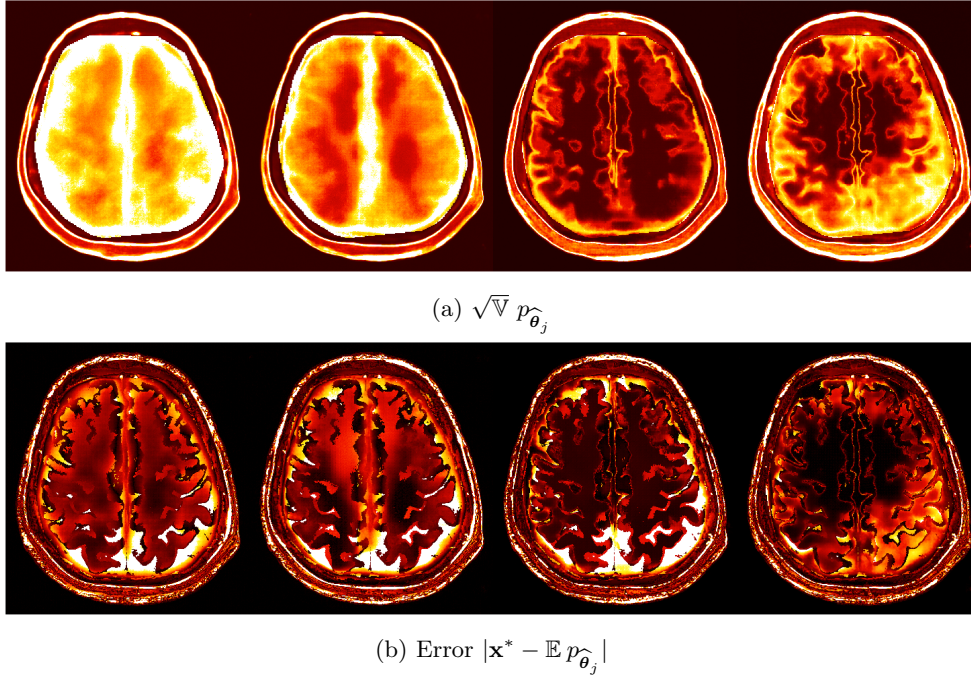


Figure 12: Posterior standard deviation compared to predictive error. (a) Posterior standard deviations of ASPIRE with increasing iterations 1 through 4 from left to right. (b) Same but with error of the posterior mean. Each ASPIRE refinement uncovers higher resolution details; furthermore the apparent correlation between the uncertainty and error increases. All plots are shown on the same colorbar from 0[m/s] to 50[m/s]

5.2. Calibration of the uncertainty

To assess the calibration of our method’s uncertainty quantification against errors, we employ the calibration test described by [68, 69]. This test involves comparisons between errors — defined by the Euclidean distance between the posterior mean estimates, $\hat{\mathbf{x}} = \mathbb{E} p_{\hat{\theta}}$, derived from samples of the posterior conditioned on the observations, \mathbf{y} , and the ground-truth parameters, \mathbf{x}^* — and the inferred uncertainty in terms of the square-root of the posterior variance, $\hat{\sigma} = \sqrt{\mathbb{V}} p_{\hat{\theta}}$. Given predictions, $\hat{\mathbf{x}}$, derived from observations, \mathbf{y} , and a measure of uncertainty, $\hat{\sigma}$, the calibration test seeks to verify the relationship:

$$\mathbb{E}_{\mathbf{x}^*, \mathbf{y}} \left[\|\mathbf{x}^* - \hat{\mathbf{x}}\|_2^2 \mid \hat{\sigma} = \sigma \right] = \sigma \quad \{\forall \sigma \in \mathbb{R} \mid \sigma \geq 0\}.$$

This expression implies that uncertainty is properly calibrated when the uncertainty is proportional to the error. For instance, if a set of gridpoints has an uncertainty of

10[m/s], their expected error should be 10[m/s]. The calibration benchmark follows as such, first the set of uncertainty values for each pixel in $\hat{\sigma} = \sqrt{V}p_{\hat{\theta}}$ is categorized into K bins of equal width, the uncertainty at each bin B_k is calculated as:

$$UQ(B_k) := \frac{1}{|B_k|} \sum_{i \in B_k} \hat{\sigma}_i$$

the average error (with $\hat{\mathbf{x}} = \mathbb{E}p_{\hat{\theta}}$) is also calculated at the same bins:

$$Error(B_k) := \frac{1}{|B_k|} \sum_{i \in B_k} (\mathbf{x}_i^* - \hat{\mathbf{x}}_i)^2.$$

The uncertainty $UQ(B_k)$ and error $Error(B_k)$ at each bin is then plotted against each other. If there is a high correlation between these values we expect the plot to match the 45°-degree angle. For details on this test see [69].

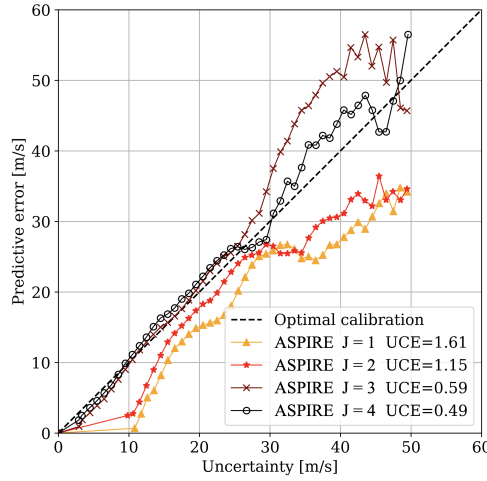


Figure 13: Calibration plot of four refinements from ASPIRE. The quality of uncertainty quantification of ASPIRE improves as measured by the calibration with respect to the error.

The resulting calibration curve from ASPIRE 4, included in Figure 13, exhibits the expected behavior by closely following the expected line. This means that our method is well calibrated for error magnitudes up to 30[m/s]. More importantly, each iterative refinement of ASPIRE improves the calibration. To quantify these improvements, we calculate the Uncertainty Calibration Error (UCE), which represents the average absolute difference between the predicted error and actual uncertainty across all bins. A lower UCE indicates a more precise calibration, and according to our experiment, ASPIRE manages to reduce the UCE by a factor of three from a value of 1.61 to 0.49. This significant improvement underscores the ability of our iterative refinement approach to produce reliable uncertainty estimates in complex imaging scenarios. By confirming the calibration of our uncertainty, we build trust in our method to properly inform downstream tasks that require access to the Bayesian posterior.

6. Discussion

Our main goal is to convince the reader of ASPIRE’s ability to close the amortization gap with iterative refinements. We were able to show that significant improvements were achieved compared to the baseline (e.g. juxtapose Figure 10a and Figure 10c). To further substantiate our claims, we place our amortized method’s performance in a broader context that includes comparisons to non-amortized inference. These comparisons illustrate our strides towards narrowing the gap between these two paradigms. Although a wide range of non-amortized VI techniques are available, our application in medical ultrasound presents unique requirements and challenges — absence of an analytical prior and the need for short time-to-solution challenged by the computational intensity of the forward/adjoint operators — limit our options for comparison. For this reason, we selected two methods: the mean-field approximation and a non-amortized normalizing flow. Through this comparative analysis, we aim to highlight our method as an efficient alternative to scenarios where non-amortized methods may be impeded by computational demands.

6.1. Mean-field approximation

Perhaps, the method with the most comparable aims in the current literature for uncertainty quantification in TUCT is the recent work by [70]. This approach employs a mean-field approximation of the posterior, and assumes the posterior covariance matrix to be diagonal for computational reasons. While understandable from a computational perspective, the established FWI literature cautions against this assumption because of the non-diagonal nature of the wave-equation Hessian [62], which introduces correlations in the errors. Our method does not make statistical assumptions on the prior or likelihood and is designed to capture the complete statistics of the posterior distribution, including long-range correlations in the covariance as evidenced in Figure 5.

Given a single set of observations, \mathbf{y}^{obs} the mean-field algorithm by [70] directly outputs estimates for the posterior mean, $\boldsymbol{\mu}_m$, and point-wise posterior standard deviation, $\boldsymbol{\sigma}_m$. This approach hinges on a relative simple modification of traditional FWI — it multiplies updates of gradient-descent with a Gaussian field. Because the computational cost of the mean-field approximation roughly correspond to that of traditional FWI that includes 100s of forward and adjoint calls, we argue that our method offers a distinct computational advantage at inference time. —i.e., ASPIRE achieves online inference at approximately 1/100th the online computational cost of the mean-field approximation. For a detailed discussion on computational costs, please refer to Section 6.6 below. We also observed that the solution from the mean-field is similar to traditional FWI thus to avoid repetition we only include mean-field results.

6.2. Non-amortized inference with normalizing flows

We also compare with a non-amortized method deriving from the same prior knowledge in the form of training samples. Given the problem size and expensive to evaluate wave-physics based forward operators and gradients, these comparisons are made with respect to a novel computationally efficient inference method inspired by recent work of [13, 71]. Instead of starting from scratch with a non-informative prior [19], which proves to be computationally prohibitively expensive, the proposed approach optimizes

network weights, ϕ , of a non-amortized normalizing flow (NF), $g_\phi(\cdot)$ that acts in the latent space of a pre-trained amortized CNF, $f_{\hat{\theta}}(\cdot)$. Given a single set of observations, \mathbf{y}^{obs} , the objective reads:

$$\begin{aligned} & \underset{\phi}{\text{minimize}} \quad \mathbb{KL} (p(h_\phi(\mathbf{z})) \parallel p(\mathbf{z} \mid \mathbf{y}^{\text{obs}})) \\ & = \mathbb{E}_{\mathbf{z} \sim \mathcal{N}(\mathbf{0}, \mathbf{I})} \left[\frac{1}{2\sigma^2} \left\| \mathcal{F} \circ f_{\hat{\theta}}^{-1} (g_\phi(\mathbf{z}); \bar{\mathbf{y}}^{\text{obs}}) - \mathbf{y}^{\text{obs}} \right\|_2^2 \right. \\ & \quad \left. + \frac{1}{2} \|g_\phi(\mathbf{z})\|_2^2 - \log |\det \mathbf{J}_{g_\phi}(\mathbf{z})| \right]. \end{aligned} \quad (7)$$

The $f_{\hat{\theta}}(\cdot)$ denotes the pre-trained CNF, optimized as per Equation 3 and $|\det \mathbf{J}_{g_\phi}|$ is the determinant of the second network’s Jacobian. By minimizing this objective, the network $g_\phi(\cdot)$ is trained to generate latent codes that further minimize residuals in data-misfit objective, which involves the nonlinear forward operator, and a ℓ_2 -norm penalty term, which ensures that the network output stays close to Gaussian distributed, therefore respecting the prior defined by the pre-trained network $f_{\hat{\theta}}(\cdot)$. To avoid having to calculate the forward map and its gradient at each iteration, we follow [72] and replace the strong constraint in 7 by a weak constraint that allows for an outer-inner-loop optimization algorithm. The optimization alternates between an expensive outer loop with L iterations inside $\{++\text{during}++\}$ which $L_{\text{inner}} \gg L$ iterations of an inexpensive inner loop are performed. The forward operator and its gradients are only calculated once during each outer loop iteration while the inner loop contains several updates to the networks. Through Monte-Carlo approximation of the above expectation, we arrive at this weak formulation by introducing N_p slack variables, $\mathbf{x}_{1:N_p}$, that alongside the network weights are minimized in the following objective:

$$\begin{aligned} & \underset{\mathbf{x}_{1:N_p}, \phi}{\text{minimize}} \quad \frac{1}{N_p} \sum_{n=0}^{N_p} \left[\frac{1}{2\sigma^2} \left\| \mathcal{F}(\mathbf{x}^{(n)}) - \mathbf{y}^{\text{obs}} \right\|_2^2 + \frac{1}{2\gamma^2} \left\| \mathbf{x}^{(n)} - f_{\hat{\theta}}^{-1} (g_\phi(\mathbf{z}^{(n)}); \bar{\mathbf{y}}^{\text{obs}}) \right\|_2^2 \right. \\ & \quad \left. + \frac{1}{2} \|g_\phi(\mathbf{z}^{(n)})\|_2^2 - \log |\det \mathbf{J}_{h_\phi}(\mathbf{z}^{(n)})| \right] \end{aligned} \quad (8)$$

where γ is the slack factor and if $\gamma \rightarrow 0$ the strong formulation is recovered. We treat the result of this optimization as the “gold standard” since it produces the best results but needs access to prior samples and to a large amount of non-amortized compute in the form of forward and adjoint PDE solves.

To assess the efficacy of posterior inference between our amortized methods and the non-amortized methods, we devised benchmarks inspired by the prescriptions in [31] to accelerate the incremental development of this class of algorithms. Firstly, we evaluate the image reconstruction quality of the point estimate generated by each method. Secondly, we conduct a qualitative review of the uncertainty images they produce. Lastly, we quantitatively analyze their uncertainty calibration using the same calibration test outlined in Section 5.2. Due to the expensive nature of the non-amortized methods, we are only able to compare results on a single unseen observation, but we expect these results to generalize to other observations.

6.3. Benchmark I: Comparing reconstruction quality

Our first comparison evaluates the posterior means from each method against the ground truth. Note, the mean-field approximation method yields estimates for posterior mean, $\boldsymbol{\mu}_m$, directly, whereas the normalizing flow-based methods estimate the posterior mean from samples. From Figure 14, we observe that the mean-field estimate contains strong artifacts in the soft tissue due to overfitting the noise as it lacks prior knowledge. As expected, our non-amortized normalizing flow method’s posterior mean exhibits a superior point estimate compared to our amortized approach. However, this improvement comes with significantly higher computational costs since this result requires 800 online evaluations of the forward operator and its adjoint when solving the optimization in Equation (8), compared to only four online evaluations for amortized ASPIRE 4. This difference in computational expense highlights the trade-off between efficiency and point-estimate quality. This example shows we can achieve results that are close to those by the non-amortized method while using only a small fraction of the online compute.

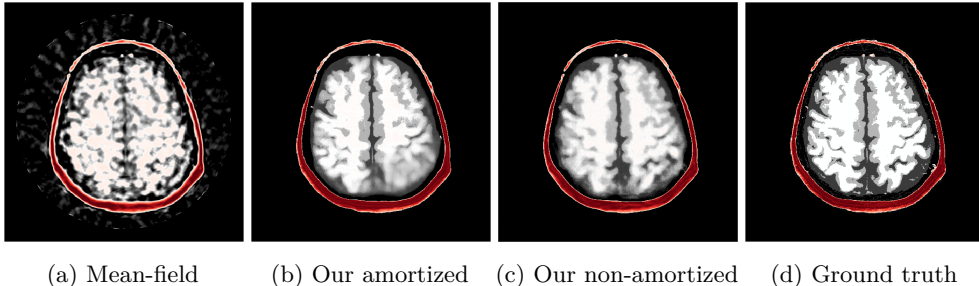


Figure 14: Reconstruction from benchmarked methods. (a) Mean-field approximation $\boldsymbol{\mu}_m$. (b) Our amortized ASPIRE 4 $\mathbb{E} p_{\hat{\theta}_4}$. (c) Our non-amortized gold standard $\mathbb{E} p_{\hat{\phi}}$. (d) Ground truth \mathbf{x}^* . As expected, the non-amortized method shows the highest quality, while our method shows similar quality albeit missing some details on the lower right.

6.4. Comparing uncertainty estimates

The posterior standard deviation of the methods tell a similar story to the posterior means. The structure of the standard deviation from the mean-field approximation Figure 15a comes mainly from the physics of the problem therefore correctly concentrates in the lower parts of the parameters where high-contrast has created complicated wavefield reverberations, but the method has failed to warn of errors due to noise artifacts throughout the reconstruction shown in Figure 15d.

To perform a close inspection on the uncertainty of the VI methods, we take a single trace through the posterior means (the diagonal trace going from the top left to the bottom right). Figure 16 shows that the mean-field method has large errors compared to the ground truth and that its uncertainty band does not contain the ground truth. Here we have chosen a 2σ band around the mean. On the other hand, both ASPIRE and the non-amortized method produce high-fidelity estimates of the ground truth. Furthermore, when our methods have high error, the uncertainty bands expand such that they contain the ground truth with high fidelity.

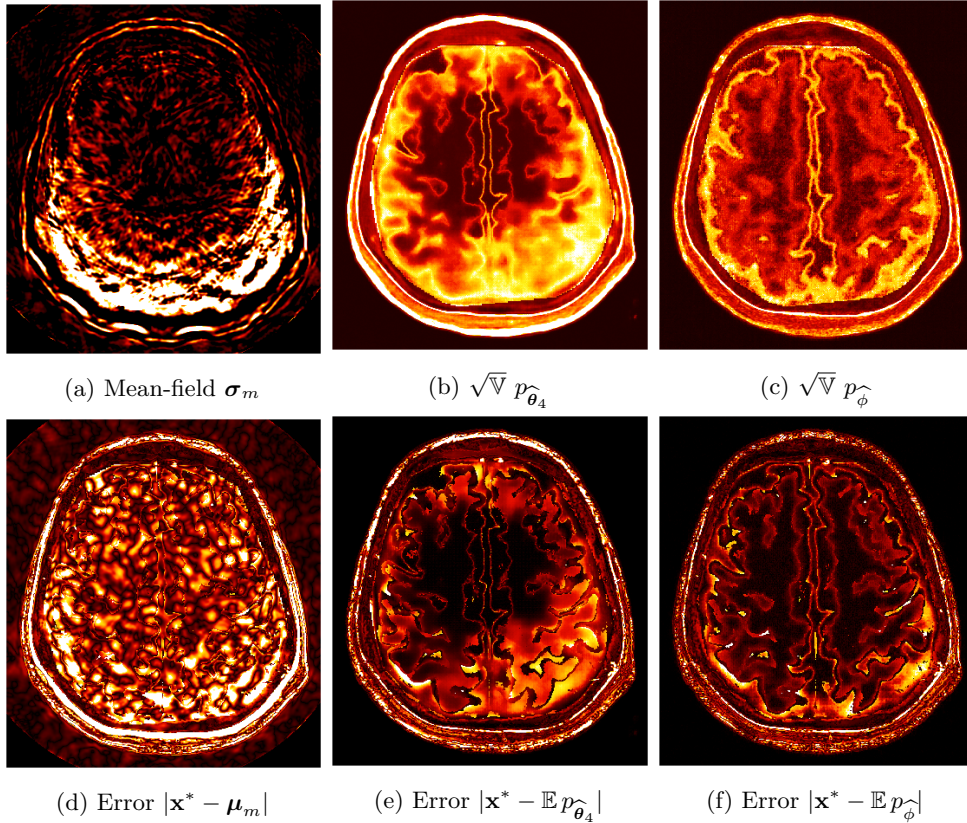


Figure 15: Comparing uncertainty of methods. The first row shows the posterior standard deviation from: (a) Non-amortized mean-field approximation sigma value. (b) Our amortized method. (c) Our non-amortized gold-standard method. The second row shows the corresponding errors. All plots have same colorbar from 0 to 50[m/s].

6.5. Benchmark II: Comparing uncertainty calibration

Following the method in Section 5.2, we compare the calibration curves of the three VI methods under consideration. Since the two non-amortized methods are compute intensive, we are only able to compute the calibration curve for a single test example Figure 14. This contrasts with the more extensive evaluation carried out in Figure 13, which encompasses a range of test cases thanks to the cheap online cost of our method. The calibration of the three methods is shown in Figure 17. We observe that the mean-field method shows poor calibration while our method achieves better calibration that is close to the one of the non-amortized method. This final observation is significant since it aligns with our thesis that we can achieve approximation quality similar to an expensive non-amortized method at a fraction of the cost. This finding highlights its computational efficiency, making it a compelling choice in scenarios where time-to-solution is a limiting factor.

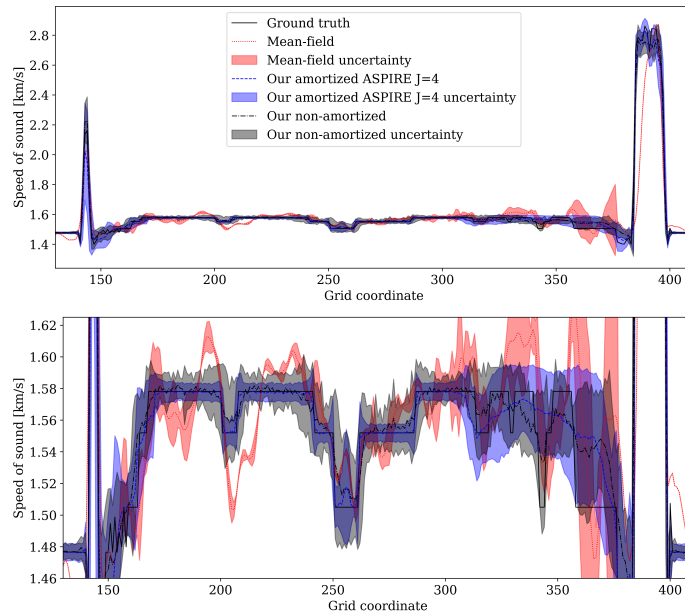


Figure 16: Comparison for a single trace. (Top figure) Estimated parameters juxtaposed with the ground truth. (Bottom figure) Same plot with zoomed vertical axis. While our posterior estimates have relatively high error in the area with coordinates 300 to 350 the uncertainty increases, suggesting the uncertainty is well calibrated.

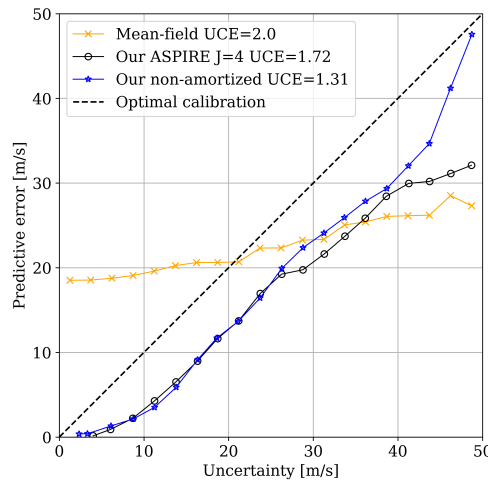


Figure 17: The mean-field approximation shows poor calibration and the gold standard non-amortized method has the best calibration as expected. Our amortized method is close to the gold standard while using a small fraction of the compute cost.

6.6. Benchmark III: Computational cost

The primary computational cost in the above methods lies in executing the physics-based forward operator \mathcal{F} and its gradient, especially in wave-based imaging where \mathcal{F} requires solving PDEs. This step is much more demanding than posterior sampling, which involves just a single neural network pass for normalizing flows. Thus, we measure computational costs in terms of PDE solves.

6.6.1. Offline phase: In amortized VI, the bulk of computational expenses occur during the offline phase. Similar to other simulation-based inference methods, synthetic observations are generated by evaluating the forward operator. Our method also requires the computation of the gradient for each training sample, which equates to two more forward operators. Additionally, each refinement requires recalculating the gradient. However, a few iterations (3-4) are generally sufficient for satisfactory results. Although the initial training phase is resource-intensive, the amortized model, once trained, becomes cost-effective with repeated use across various datasets.

6.6.2. Online phase: The main cost during the online phase is also PDE solves. Each refinement iteration, requiring gradient calculation, incurs a cost of 2 PDE solves Section 4.2.3. Compared to earlier Bayesian methods that required 1000 – 10000 online PDE solves [43], our method significantly reduces this to less than 10 PDE online solves, nearing real-time imaging. In medical applications where timely results are crucial [25], fast online inference is essential.

6.6.3. Compute break-even: Despite the high cost of the offline phase, our method becomes cost-effective after a certain number of evaluations. The break-even point can be estimated from Table 2. For instance, for TUCT, compared to a mean-field solution requiring 600 PDE solves, our method—with $N = 1000$ and $J = 4$ —incurs 9000 offline and 8 online PDE solves for a total of 9008 PDE solves. Thus becomes cost-effective after about 15 test cases, not accounting for improved estimates and uncertainty.

When juxtaposed with our proposed gold-standard non-amortized method, our amortized approach breaks-even more rapidly. For the non-amortized method, we use a pretrained ASPIRE 1 network, which requires $1000 + 2 \times 1000 \times 1 = 3000$ offline PDEs solves, followed by $2 \times 1 = 2$ online solves. The optimization of (8) uses $L = 400$ outer loop iterations leading to online 800 PDE solves. The total cost is 3802 PDE solves, which means the amortized method pays itself back when used on $\frac{9008}{3802} \approx 3$ test cases.

Table 2: Costs measured by evaluations of forward/adjoint operator.

Method	Offline cost	Online cost
ASPIRE	$N + 2 \times N \times J$	$2 \times J$
Our non-amortized method	$N + 2 \times N \times J$	$2 \times J + 2 \times L$
Mean-field approximation	None	$2 \times L$

7. Related work

A precursor to our work, [23] introduced the concept of the summary network, which acts on the condition and is optimized under the same objective as the normalizing flow. Our approach extends this concept into what we term a “physical summary network,” where each refinement iteration enhances the summary statistic by improving the fiducial quality. Although not iterative and for different modalities [73] demonstrated one of the first uses of CNFs for medical imaging.

During the preparation of this manuscript, we identified closely related research [74], which proposes a method for solving Bayesian inverse problems that resembles loop-unrolling augmented with Bayesian network layers. We acknowledged their contributions. However, we note key differences: [74] employ Bayesian networks that model distributions on the network weights, which can impose restrictive assumptions on the distribution families that can be learned akin to mean-field approximations. In contrast, our use of CNFs aims to directly learn the Bayesian posterior, and theoretically, as universal approximators [75, 76], offer greater flexibility. We believe our method generalizes to other conditional density estimators whereas the work in [74] is specific to Bayesian networks.

Our work also shares similarities with DEEPGEM by [77], which utilizes Expectation Maximization to solving inverse problems. Their process involves optimizing a non-amortized normalizing flow to sample from a posterior based on current nuisance parameter estimates, followed by MAP optimization. Crucially, our method is different as it is amortized, eliminating network retraining or costly MAP optimization at inference time. Additionally, our method requires few online gradients (3-4), compared to the numerous ones needed by DEEPGEM, thereby significantly reducing compute.

8. Future work

The superior posterior mean achieved by the non-amortized method compared to our solution indicates that further information could be extracted from \mathbf{y}^{obs} through additional refinement iterations. Although we proposed some heuristics, determining the optimal number of refinement iterations to maximize performance remains an area of research. Our technique is compatible with any conditional density estimator. While we have utilized Normalizing Flows in our implementation, the framework can easily adapt to other conditional density estimators such as Variational Autoencoders (VAEs) [78], GANs [79] diffusion models [80].

Due to out-of-plane effects of acoustic modeling, the TUCT problem is best treated in 3D [47]. Although TUCT was demonstrated here in 2D, ASPIRE is not limited to 2D problems. Particularly, when empowered by memory-frugal normalizing flows [33] ASPIRE can achieve full volume Bayesian inference for 3D inverse problems. For our TUCT example, the limiting factor was the absence of a 3D training dataset but in seismic imaging (a field that appreciates the importance of 3D modeling and inference) we used the 3D Compass dataset [81] and share the results of solving 3D FWI in Figure 18. Setup details are similar to the TUCT problem. A detailed study of the 3D capabilities of ASPIRE is being prepared for future work but here we succinctly report that for a $128 \times 128 \times 128$ inference problem, offline training took 1 day on a single GPU and that the uncertainties shown in Figure 18e were pleasingly correlated

with structures that are known to be difficult to image i.e. structures that are: deeper, vertical or close to the edge.

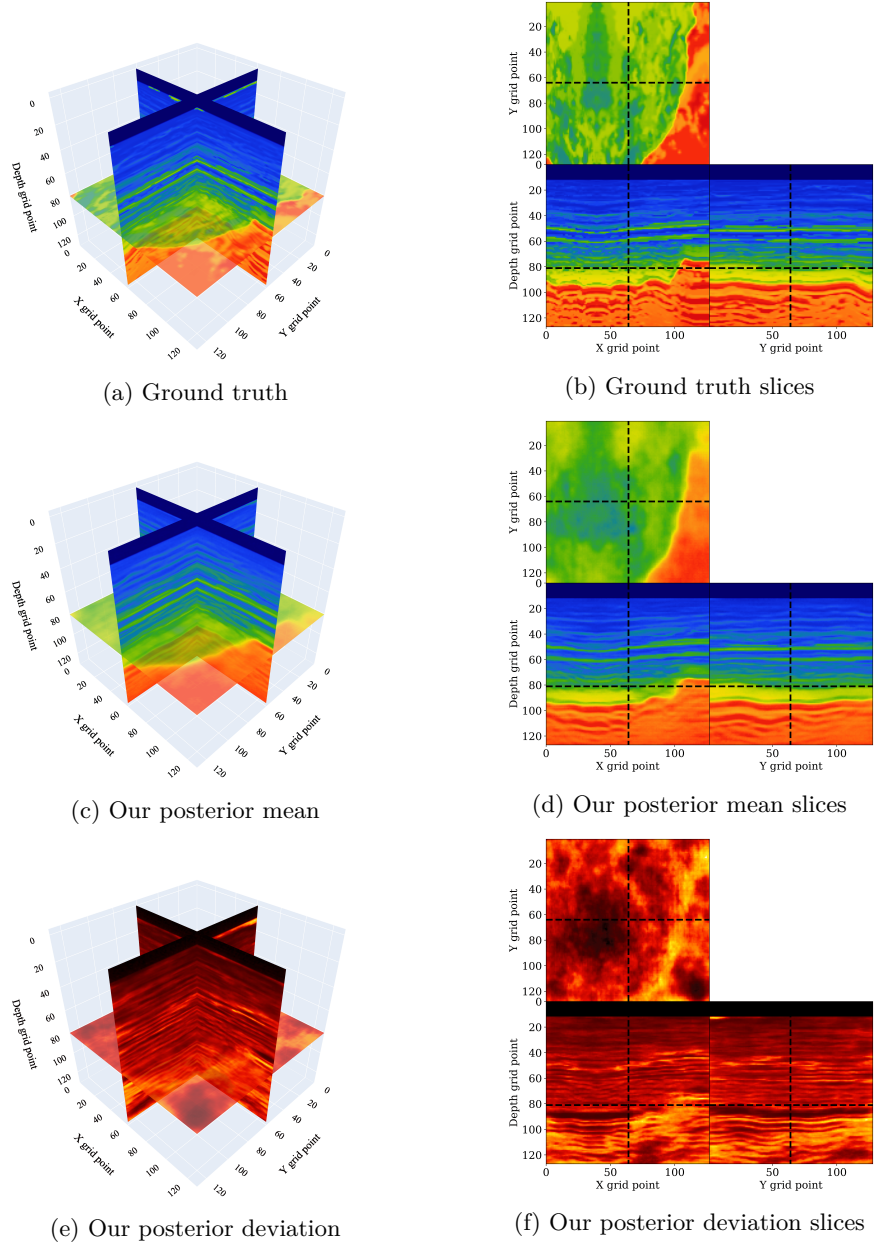


Figure 18: ASPIRE for 3D inverse problems. (a) Ground truth 3D render. (b) Ground truth folded out slices. (c) Our posterior mean 3D render. (d) Posterior mean slices. (e) Our posterior deviation 3D render. (f) Posterior deviation slices. The ASPIRE 2 shows physically viable probabilistic estimates for a $128 \times 128 \times 128$ FWI problem.

9. Conclusions

We introduced a method that iteratively improves on approximations to Bayesian posteriors in the context of inverse problems. Our method brings together concepts from generative modeling, physics-hybrid methods, and statistics. Practically our algorithm achieves higher performance by iteratively extracting more information from the observed data. The mathematical interpretation of our method is to make a score-based summary statistic more informative by moving the fiducial points closer to the maximum likelihood estimates. Our method forms an interesting middle ground between amortized VI and non-amortized VI. Importantly, the offline training phase makes it such that the online costs are small rendering our approach suitable for applications that demand fast online turn-around times. Our experiments demonstrate improvements in estimated posteriors on a stylized example where the posterior is known analytically. In a realistic medical transcranial ultrasound imaging application, the online cost is many times cheaper than non-amortized methods while demonstrating high-quality amortized inference. We believe that this approach represents a step forward in the field, offering a computationally efficient solution for Bayesian inference in high-dimensional inverse problems with expensive to evaluate forward operators.

10. Availability of data and materials

The scripts and datasets to reproduce the experiments are available on the GitHub page ASPIRE.jl.

11. Acknowledgements

This research was carried out with the support of Georgia Research Alliance and partners of the ML4Seismic Center. The authors gratefully acknowledge the contribution of OpenAI’s ChatGPT for refining sentence structure and enhancing the overall readability of this manuscript. After using this service, the authors reviewed and edited the content as needed and take full responsibility for the content of the publication.

Appendix A. FASTMRI acoustic dataset creation

Based off of the MRI dataset [57], we manually assigned acoustic values to MRI intensities by following the table of acoustic brain tissue properties in the supplemental section of [47]. Although MRI intensities are not necessarily related to acoustic tissue properties, we found that we could produce reasonably realistic acoustic parameters as compared to the acoustic parameters from the MIDA volume. In Figure A1, we show some example training acoustic parameters. We also plot the average and standard variation between all 1000 training samples in Figure A2. From these plots, we note that there are few similarities between training examples apart from the biologically consistent human brain structures.

Appendix B. Wave modeling and FWI implementation

To mask source-receiver artifacts, the gradients used for the traditional FWI optimizations are masked by a binary matrix where the mask was made large enough

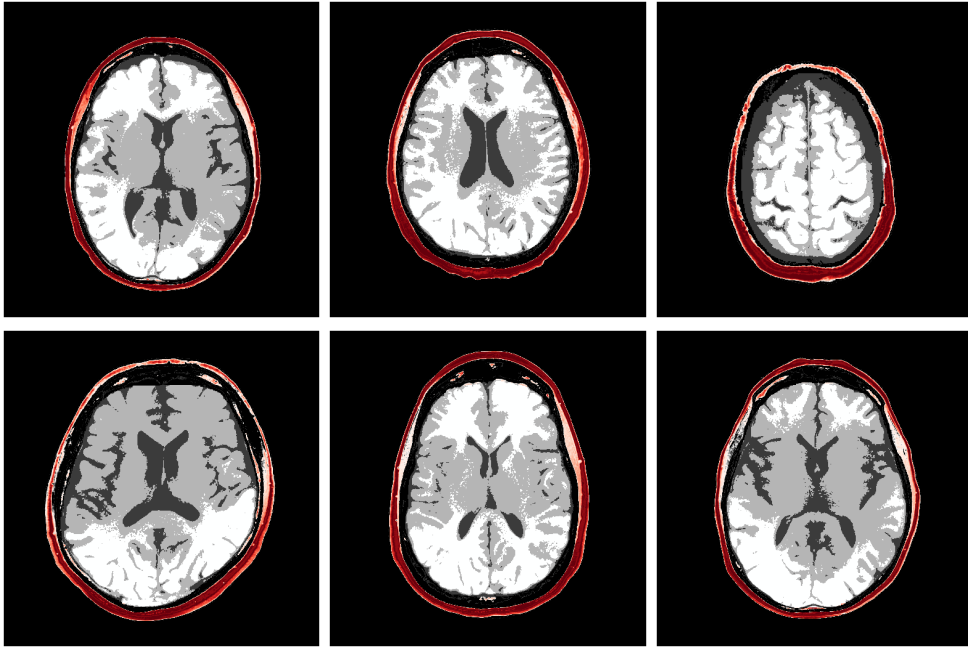


Figure A1: Examples of training examples used to train our method $\mathbf{x}^{(n)} \sim p(\mathbf{x})$.

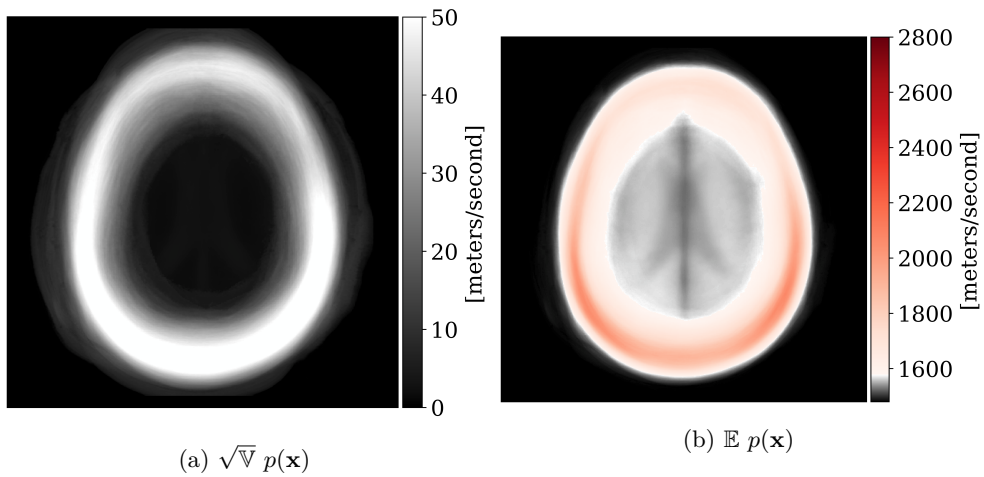


Figure A2: Training dataset used to train models. (a) Standard deviation of samples. (b) Mean of samples.

to include the skull but otherwise assumed no knowledge of the skull. We also avoid the inverse crime by generating any “observed” acoustic data with a spatial finite-difference kernel of size 16 gridpoints and with computational time discretization of 0.025 microseconds while the physical operator used for gradient calculation corresponds to a simulation with spatial finite-difference kernel of size 8 gridpoints and computational time discretization of 0.5 microseconds.

Appendix C. Conditional normalizing flow training

We implement a conditional normalizing flow with an architecture that consists of 3 multiscale levels as in RealNVP [32] and each level contains 9 conditional coupling layers similar to C-INN layers [82] and also GLOW learned channel permutations [83]. The learned network in the coupling layers is a 3 layer convolutional resnet where each convolutional block has 64 hidden channels. As a summary network, we used a 4 level UNet. In total, the network is made out of 6,913,326 parameters. The optimization is stochastic gradient descent with batch size of 8 and an ADAM [83] optimizer with learning rate of $8e - 4$. Following the work of [82, 84], we added Gaussian noise to the target images with standard deviation of 0.01. We trained the network until the objective did not improve on a leave-out validation set. The network architecture implementation and training code can found in the github ASPIRE.jl.

Appendix D. More posterior samples

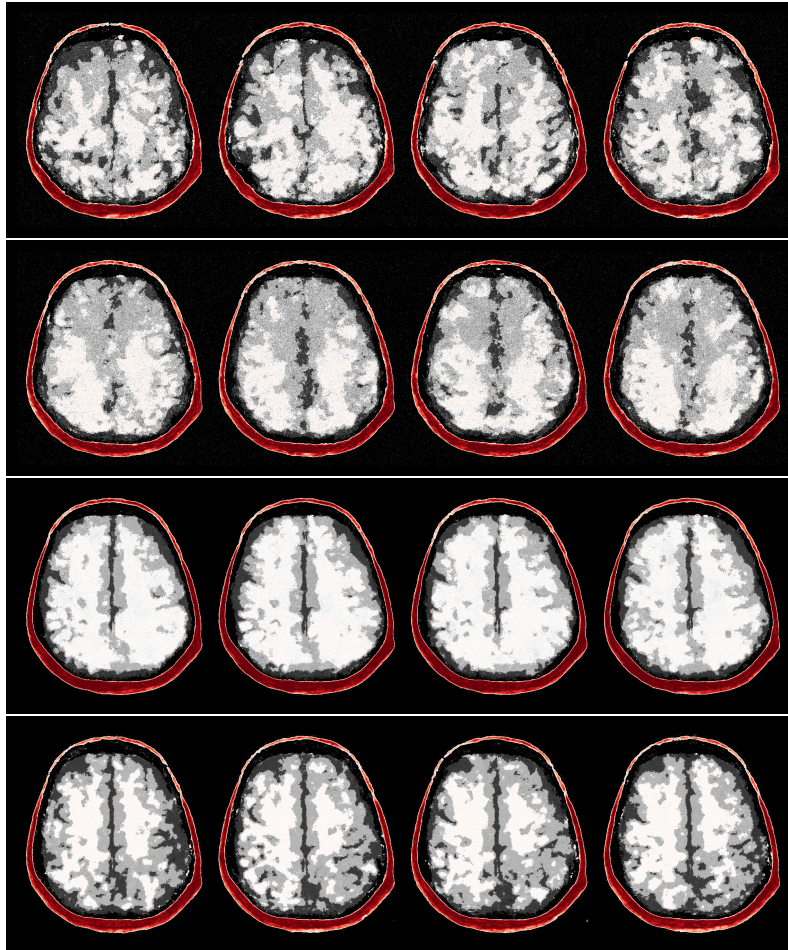


Figure D1: Posterior sampling for four iterations of ASPIRE. First row is ASPIRE 1, second row is ASPIRE 2 and so on until the last row showing results from ASPIRE 4. Each refinement visually improves the quality and agreement of the posterior samples.

Appendix E. Selecting number of posterior samples

From posterior samples, Monte Carlo estimates of the posterior statistics can be calculated. As short hand, statistic estimates from the distribution p are:

$$\mathbb{E} p := \mathbb{E}_{\mathbf{x} \sim p(\mathbf{x}|\mathbf{y})} [\mathbf{x}] \quad (\text{E.1})$$

$$\sqrt{\mathbb{V}} p := \sqrt{\mathbb{E}_{\mathbf{x} \sim p(\mathbf{x}|\mathbf{y})} [(\mathbf{x} - \mathbb{E} p)^2]}. \quad (\text{E.2})$$

For example, the posterior mean calculated from samples from the above trained approximate posterior $p_{\hat{\theta}}$ is referred to as $\mathbb{E}p_{\hat{\theta}}$.

We calculated empirical means and standard deviations using 512 samples, but due to the efficiency of our method (10ms per sample), a larger number of samples could be rapidly generated. We chose the quantity 512 due to the convergence of quality metrics over number of posterior samples as shown in Figure E1.

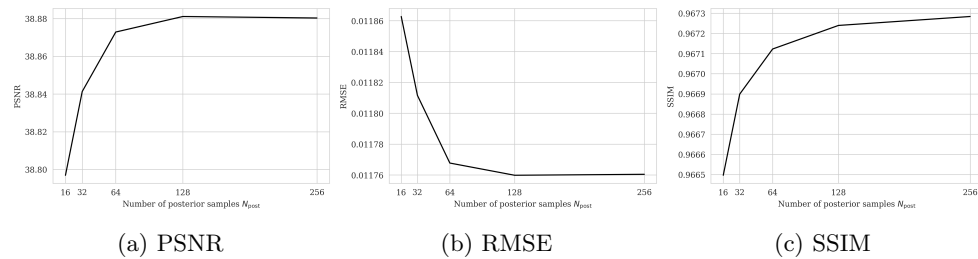


Figure E1: Quality metrics of the posterior mean converge between 256 and 512 posterior samples.

References

- [1] Hadamard J 1902 *Princeton university bulletin* 49–52
- [2] Tarantola A 2005 *Inverse problem theory and methods for model parameter estimation* (SIAM)
- [3] Gelman A, Carlin J B, Stern H S and Rubin D B 1995 *Bayesian data analysis* (Chapman and Hall/CRC)
- [4] Curtis A and Lomax A 2001 *Geophysics* **66** 372–378
- [5] Bishop C M and Nasrabadi N M 2006 *Pattern recognition and machine learning* vol 4 (Springer)
- [6] Robert C P, Casella G and Casella G 1999 *Monte Carlo statistical methods* vol 2 (Springer)
- [7] Siahkoobi A, Rizzuti G and Herrmann F J 2022 *Geophysics* **87** S281–S302
- [8] Martin J, Wilcox L C, Burstedde C and Ghattas O 2012 *SIAM Journal on Scientific Computing* **34** A1460–A1487
- [9] Dempster A P, Laird N M and Rubin D B 1977 *Journal of the royal statistical society: series B (methodological)* **39** 1–22
- [10] Tierney L and Kadane J B 1986 *Journal of the american statistical association* 82–86
- [11] Jordan M I, Ghahramani Z, Jaakkola T S and Saul L K 1999 *Machine learning* **37** 183–233
- [12] Kullback S and Leibler R A 1951 *The annals of mathematical statistics* **22** 79–86

- [13] Siahkoochi A, Rizzuti G, Orozco R and Herrmann F J 2023 *Geophysics* **88** R297–R322
- [14] Siahkoochi A, Rizzuti G, Louboutin M, Witte P A and Herrmann F J 2021 *arXiv preprint arXiv:2101.03709*
- [15] Feng B T, Smith J, Rubinstein M, Chang H, Bouman K L and Freeman W T 2023 *arXiv preprint arXiv:2304.11751*
- [16] Welling M and Teh Y W 2011 Bayesian learning via stochastic gradient langevin dynamics *Proceedings of the 28th international conference on machine learning (ICML-11)* (Citeseer) pp 681–688
- [17] Sun H and Bouman K L 2021 Deep probabilistic imaging: Uncertainty quantification and multi-modal solution characterization for computational imaging *Proceedings of the AAAI Conference on Artificial Intelligence* vol 35 pp 2628–2637
- [18] Liu Q and Wang D 2016 *Advances in neural information processing systems* **29**
- [19] Zhang X, Lomas A, Zhou M, Zheng Y and Curtis A 2023 *Geophysical Journal International* **234** 546–561
- [20] Blatter D, Morzfeld M, Key K and Constable S 2022 *Geophysical Journal International* **231** 1057–1074
- [21] Bardsley J M, Solonen A, Haario H and Laine M 2014 *SIAM Journal on Scientific Computing* **36** A1895–A1910
- [22] Cremer C, Li X and Duvenaud D 2018 Inference suboptimality in variational autoencoders *International Conference on Machine Learning* (PMLR) pp 1078–1086
- [23] Radev S T, Mertens U K, Voss A, Ardizzone L and Köthe U 2020 *IEEE transactions on neural networks and learning systems*
- [24] Putzky P *et al.* 2023
- [25] Bauer S, Seitel A, Hofmann H, Blum T, Wasza J, Balda M, Meinzer H P, Navab N, Hornegger J and Maier-Hein L 2013 Real-time range imaging in health care: a survey *Time-of-Flight and Depth Imaging. Sensors, Algorithms, and Applications* (Springer) pp 228–254
- [26] Marino J, Yue Y and Mandt S 2018 Iterative amortized inference *International Conference on Machine Learning* (PMLR) pp 3403–3412
- [27] Whang J, Lindgren E and Dimakis A 2021 Composing normalizing flows for inverse problems *International Conference on Machine Learning* (PMLR) pp 11158–11169
- [28] Orozco R, Siahkoochi A, Rizzuti G, van Leeuwen T and Herrmann F J 2021 Photoacoustic imaging with conditional priors from normalizing flows *NeurIPS 2021 Workshop on Deep Learning and Inverse Problems*
- [29] Grcić M, Grubišić I and Šegvić S 2021 *Advances in Neural Information Processing Systems* **34** 23968–23982

- [30] Shorten C and Khoshgoftaar T M 2019 *Journal of big data* **6** 1–48
- [31] Donoho D 2023 *arXiv preprint arXiv:2310.00865*
- [32] Dinh L, Sohl-Dickstein J and Bengio S 2016 *arXiv preprint arXiv:1605.08803*
- [33] Orozco R, Witte P, Louboutin M, Siahkoochi A, Rizzuti G, Peters B and Herrmann F J 2023 *arXiv preprint arXiv:2312.13480*
- [34] Kovachki N, Baptista R, Hosseini B and Marzouk Y 2020 *arXiv preprint arXiv:2006.06755*
- [35] Deans M C 2002 Maximally informative statistics for localization and mapping *Proceedings 2002 IEEE International Conference on Robotics and Automation (Cat. No. 02CH37292)* vol 2 (IEEE) pp 1824–1829
- [36] Heavens A F, Jimenez R and Lahav O 2000 *Monthly Notices of the Royal Astronomical Society* **317** 965–972
- [37] Alsing J and Wandelt B 2018 *Monthly Notices of the Royal Astronomical Society: Letters* **476** L60–L64
- [38] Alsing J, Wandelt B and Feeney S 2018 *Monthly Notices of the Royal Astronomical Society* **477** 2874–2885
- [39] Brehmer J, Louppe G, Pavez J and Cranmer K 2020 *Proceedings of the National Academy of Sciences* **117** 5242–5249
- [40] Van Leeuwen T and Herrmann F J 2013 *Geophysical Journal International* **195** 661–667
- [41] Casella G and Berger R L 2002 *Duxbury press*
- [42] Adler J and Öktem O 2018 *arXiv preprint arXiv:1811.05910*
- [43] Zhao X, Curtis A and Zhang X 2022 *Geophysical Journal International* **228** 213–239
- [44] Robins T, Camacho J, Agudo O C, Herraiz J L and Guasch L 2021 *Sensors* **21** 4570
- [45] Wang K, Matthews T, Anis F, Li C, Duric N and Anastasio M A 2015 *IEEE transactions on ultrasonics, ferroelectrics, and frequency control* **62** 475–493
- [46] Williamson P 1991 *Geophysics* **56** 202–207
- [47] Guasch L, Calderón Agudo O, Tang M X, Nachev P and Warner M 2020 *NPJ digital medicine* **3** 1–12
- [48] Robins T C, Cueto C, Cudeiro J, Bates O, Agudo O C, Strong G, Guasch L, Warner M and Tang M X 2023 *Ultrasound in Medicine & Biology* **49** 2302–2315
- [49] Thomson H 2023 *Ultrasonic differentiation of healthy and cancerous neural tissue* Ph.D. thesis University of Glasgow
- [50] Cueto C, Guasch L, Cudeiro J, Agudo Ò C, Robins T, Bates O, Strong G and Tang M X 2021 *IEEE Transactions on Ultrasonics, Ferroelectrics, and Frequency Control* **69** 27–37

- [51] Espin I, Salaun N, Jiang H and Reinier M 2023 *The Leading Edge* **42** 16–23
- [52] Marty P, Boehm C and Fichtner A 2021 Acoustoelastic full-waveform inversion for transcranial ultrasound computed tomography *Medical Imaging 2021: Ultrasonic Imaging and Tomography* vol 11602 (SPIE) pp 210–229
- [53] Esser E, Guasch L, Herrmann F J and Warner M 2016 *The Leading Edge* **35** 235–239
- [54] Esser E, Guasch L, van Leeuwen T, Aravkin A Y and Herrmann F J 2018 *SIAM Journal on Imaging Sciences* **11** 376–406
- [55] Guasch L, Warner M and Ravaut C 2019 *Geophysics* **84** R447–R461
- [56] Iacono M I, Neufeld E, Akinagbe E, Bower K, Wolf J, Vogiatzis Oikonomidis I, Sharma D, Lloyd B, Wilm B J, Wyss M *et al.* 2015 *PloS one* **10** e0124126
- [57] Zbontar J, Knoll F, Sriram A, Murrell T, Huang Z, Muckley M J, Defazio A, Stern R, Johnson P, Bruno M *et al.* 2018 *arXiv preprint arXiv:1811.08839*
- [58] Louboutin M, Lange M, Luporini F, Kukreja N, Witte P A, Herrmann F J, Velesko P and Gorman G J 2019 *Geoscientific Model Development* **12** 1165–1187 URL <https://www.geosci-model-dev.net/12/1165/2019/>
- [59] Luporini F, Louboutin M, Lange M, Kukreja N, Witte P, Hüchelheim J, Yount C, Kelly P H J, Herrmann F J and Gorman G J 2020 *ACM Trans. Math. Softw.* **46** ISSN 0098-3500 URL <https://doi.org/10.1145/3374916>
- [60] Witte P A, Louboutin M, Kukreja N, Luporini F, Lange M, Gorman G J and Herrmann F J 2019 *Geophysics* **84** F57–F71
- [61] Plessix R E 2006 *Geophysical Journal International* **167** 495–503
- [62] Virieux J and Operto S 2009 *Geophysics* **74** WCC1–WCC26
- [63] Orozco R, Siahkoohi A, Rizzuti G, van Leeuwen T and Herrmann F J 2023 Adjoint operators enable fast and amortized machine learning based bayesian uncertainty quantification *Medical Imaging 2023: Image Processing* vol 12464 (SPIE) pp 357–367
- [64] Mukherjee S, Carioni M, Öktem O and Schönlieb C B 2021 *Advances in Neural Information Processing Systems* **34** 21413–21425
- [65] Marty P, Boehm C and Fichtner A 2023 Shape optimization for transcranial ultrasound computed tomography *Medical Imaging 2023: Ultrasonic Imaging and Tomography* vol 12470 (SPIE) pp 77–88
- [66] Ghosal S and Van der Vaart A 2017 *Fundamentals of nonparametric Bayesian inference* vol 44 (Cambridge University Press)
- [67] Barbano R, Arridge S, Jin B and Tanno R 2022 Uncertainty quantification in medical image synthesis *Biomedical Image Synthesis and Simulation* (Elsevier) pp 601–641
- [68] Guo C, Pleiss G, Sun Y and Weinberger K Q 2017 On calibration of modern neural networks *International conference on machine learning* (PMLR) pp 1321–1330

- [69] Laves M H, Ihler S, Fast J F, Kahrs L A and Ortmaier T 2020 Well-calibrated regression uncertainty in medical imaging with deep learning *Medical Imaging with Deep Learning* (PMLR) pp 393–412
- [70] Bates O, Guasch L, Strong G, Robins T C, Calderon-Agudo O, Cueto C, Cudeiro J and Tang M 2022 *Inverse Problems* **38** 045008
- [71] Detommaso G, Kruse J, Ardizzone L, Rother C, Köthe U and Scheichl R 2019 *stat* **1050** 25
- [72] Siahkoohi A, Rizzuti G and Herrmann F J 2020 Weak deep priors for seismic imaging *SEG Technical Program Expanded Abstracts 2020* (Society of Exploration Geophysicists) pp 2998–3002
- [73] Denker A, Schmidt M, Leuschner J and Maass P 2021 *Journal of Imaging* **7** 243
- [74] Barbano R, Zhang C, Arridge S and Jin B 2021 Quantifying model uncertainty in inverse problems via bayesian deep gradient descent *2020 25th International Conference on Pattern Recognition (ICPR)* (IEEE) pp 1392–1399
- [75] Teshima T, Ishikawa I, Tojo K, Oono K, Ikeda M and Sugiyama M 2020 *Advances in Neural Information Processing Systems* **33** 3362–3373
- [76] Draxler F, Kühmichel L, Rousselot A, Müller J, Schnörr C and Köthe U 2023 *arXiv preprint arXiv:2306.13520*
- [77] Gao A, Castellanos J, Yue Y, Ross Z and Bouman K 2021 *Advances in Neural Information Processing Systems* **34** 11592–11603
- [78] Sohn K, Lee H and Yan X 2015 *Advances in neural information processing systems* **28**
- [79] Mirza M and Osindero S 2014 *arXiv preprint arXiv:1411.1784*
- [80] Song Y, Sohl-Dickstein J, Kingma D P, Kumar A, Ermon S and Poole B 2020 *arXiv preprint arXiv:2011.13456*
- [81] Jones C, Edgar J, Selvage J and Crook H 2012 Building complex synthetic models to evaluate acquisition geometries and velocity inversion technologies *74th EAGE Conference and Exhibition incorporating EUROPEC 2012* (European Association of Geoscientists & Engineers) pp cp–293
- [82] Ardizzone L, Lüth C, Kruse J, Rother C and Köthe U 2019
- [83] Kingma D P and Ba J 2014 *arXiv preprint arXiv:1412.6980*
- [84] Tran B H, Franzese G, Michiardi P and Filippone M 2023 *arXiv preprint arXiv:2305.18900*